Engineering Fracture Mechanics 138 (2015) 265–288

Contents lists available at ScienceDirect

Engineering Fracture Mechanics

journal homepage: www.elsevier.com/locate/engfracmech

Influence of microstructure variability on short crack behavior through postulated micromechanical short crack driving force metrics

Andrea Rovinelli [a,b], Ricardo A. Lebensohn [c], Michael D. Sangid [a,*]

[a] School of Aeronautics and Astronautics, Purdue University, 701 W. Stadium Ave, West Lafayette, IN 47907-2045, USA
[b] Seconda Facoltà di Ingegneria, Alma Mater Studiorum University of Bologna, via Fontanelle 40, 47100 Forlì, FC, Italy
[c] Materials Science and Technology Division, Los Alamos National Laboratory, Los Alamos, NM 87545, USA

ARTICLE INFO

Article history:
Received 29 June 2014
Received in revised form 25 February 2015
Accepted 2 March 2015
Available online 18 March 2015

Keywords:
Microstructure variability
Short crack growth rate
Fatigue scatter
Crystal plasticity
Elasto-viscoplastic formulation

ABSTRACT

In nature, variability in the short crack (SC) growth rate is observed in polycrystalline materials, in which the evolution and distribution of the local plasticity is strongly influenced by microstructural features. Sets of different microstructure realizations are constructed, simulated and analyzed using an elasto-viscoplastic crystal plasticity model, in order to investigate the influence of some microstructure parameters on SC behavior through postulated Micromechanical Short Crack Driving Force Metrics (MSCDFMs). The results of the analysis will identify a preferred MSCDFM and then, we will close the loop hypothesizing a relationship between microstructure variability, uncertainty in fatigue behavior prediction, and MDCFMs heterogeneity.

1. Introduction

The Paris law for fatigue crack growth considers a long crack, defined in the case the material can be considered homogeneous and the plastic zone ahead of the crack tip is small compared to the characteristic length of the specimen [1]. On the other hand, short crack growth is significantly influenced by the microstructure of the material, and this influence needs to be quantified for accurate life prediction. The first authors to investigate microstructural short crack (for brevity we will refer to it as SC) growth were McEvily and Boettner [2], specifically observing that the short crack growth rate is dependent on grain orientation. Short crack advancement can be idealized as series of slip processes [3], with the criterion for dislocation emission from the crack tip outlined by Rice and Thomson [4]. Subsequently Yoder et al. [5] investigated the influence of grain size on the variability of the stress intensity factor threshold value (ΔK_{th}) in polycrystalline materials, finding that it increases proportionally to the square root of the average grain size. Navarro and de los Rios [6] proposed a model for SCG in which they assumed that the extent of the plastic zone ahead of the crack tip is confined by the first obstacles for dislocation motion, i.e. grain boundaries (GBs), and that growth rate depends on the distance between the crack tip and the obstacle itself. These studies suggest that microstructural parameters, e.g. grain orientation, grain size, distance of the crack tip from obstacles, etc., strongly influence the SC growth rate. Further, since each engineering alloy has a distribution of microstructure attributes, these features play a crucial role in determining microstructure variability in the SCG behavior. The aim of the present work, and also its novelty, is to begin to investigate the relationship between the variability of certain

* Corresponding author.
E-mail address: msangid@purdue.edu (M.D. Sangid).

http://dx.doi.org/10.1016/j.engfracmech.2015.03.001
0013-7944/

Nomenclature

a	crack length
$\boldsymbol{C}$	stiffness tensor
$h_{\alpha\beta}$	hardening interaction matrix
k	Fatemi–Socie weight parameter for normal stress
$\boldsymbol{m}$	slip direction vector
D1, D3, D5	MSCDF representing slip system with the maximum accumulated plastic resolved shear-strain, total accumulated plastic resolved shear-strain in a voxel, and maximum accumulated plastic shear strain amongst planes subjected to tensile normal stresses, respectively
E1, E3, E5	energetic MSCDF equivalent of D1, D3, D5, respectively
$E^{max}_{imposed}$	Imposed maximum macroscopic strain tensor
$\boldsymbol{M}$	symmetric par of the Schmid' tensor
$\boldsymbol{n}$	normal to the slip plane vector
N^{MSCDFM}	total number of MSCDF
$Nsim$	total number of realizations
$S_{imposed}$	Imposed macroscopic stress tensor
$\boldsymbol{x}$	global Cartesian position
$\boldsymbol{\sigma}$	Cauchy stress tensor
α	slip system index
$\dot{\gamma}^{\alpha}$	shear strain rate for α^{th} slip system
$\dot{\gamma}_0$	single crystal reference shear strain rate
Γ^{α}	accumulated shear strain on the α^{th} slip system
Γ^{α}_{hard}	weighted sum of accumulated plastic shear strain
Δt	time increment
$\Delta\theta$	minimum absolute value of misalignment between the FIP maximum direction and adjacent slip-plane/principal stress axis at a given strain level
$\overline{\Delta\theta}$	average misalignment between the FIP maximum direction and adjacent slip-plane/principal stress axis through all the realizations at a given strain level
$\overline{\overline{\Delta\theta}}$	averaged FIPs maximum direction angle and adjacent slip-plane/principal stress axis through all the different FIPs at a given strain level
$\boldsymbol{\varepsilon}, \boldsymbol{\varepsilon}^{pl}, \dot{\boldsymbol{\varepsilon}}^{pl}$	Lagrangian strain, plastic strain, plastic strain rate tensor
θ	maximum FIP direction on the plane perpendicular to the crack plane passing through the ellipse small axis
θ_0, θ_1	single crystal stiffness ab initio and asymptotic
σ^p_n	normal stress acting on slip plane p
$\tau, \tau_{\mathrm{CRSS}}$	resolved and critical resolved shear stress
τ_0, τ_1	single crystal reference critical resolved shear stress ab initio and asymptotic
φ	maximum FIP direction in the crack plane

microstructure features (i.e. grain orientation), local computed micromechanical fields associated with SC growth rate and hypothesized Micromechanical Short Crack Driving Force Metrics (MSCDFMs), using high-resolution simulations, and then postulating a relationship between SC growth rate and MSCDFMs. Specifically, the effect of the orientation of the cracked grain and the crack length on various MSCDFMs that involve local stress and strain fields are studied.

In recent years, researchers have started to use crystal plasticity (CP) models (e.g. Asaro [7]) combined with powerful computational tools, allowing researchers to study the effect of the local microstructure features on the local stress and strain fields, to attempt to model the effect of microstructural parameters on SC behavior. Building upon the model proposed by Navarro and de los Rios [6], Wilkinson [8] studied the interaction between the crack tip and the closest GB, as a function of distance. Their results showed that while the crack tip is in the core of a grain, the growth rate is almost constant, and, as the crack impinges upon a GB, the growth rate is dependent on the neighboring grain's misorientation. Several other authors implemented 2D CP simulations on simplified microstructures. Ferrie et al. [9] investigated the relationship between Stage I crack growth rate and the orientation of the neighboring grain through the calculation of crack tip opening displacement and crack tip sliding displacement, finding an orientation dependence. Potirniche et al. [10] showed that variability in SC growth rate could be reproduced in simulations changing the orientation of the neighboring grain. These studies serve as the basis for understanding complex SC behavior and emphasize the need to explore the complete space of complex 3-D behavior, due to the interaction of multiple microstructure attributes, such as grain clustering which constitutes an important feature for fatigue analysis [11,12].

To achieve a better understanding of the physics of SC growth, many researchers investigated the role of dislocations. Experiments conducted by George and Michot [13] show that the most common source of dislocations at the crack tip, is one that emits dislocations with multiple Burgers vectors on different glide planes simultaneously. To simulate this behavior, many researchers have utilized molecular dynamics (MD) simulations. Bitzek and Gumbsch [14] and Zhang and Ghosh [15]

investigated the dependence of dislocation emission, multiplication and interaction at the crack tip in a single crystal. These simulations showed the importance of dislocation type and crystal orientation on crack growth. Moreover, Sangid et al. [16] investigated the role of GBs in slip transmission and dislocation nucleation, observing that the GB character introduces variability in the response of the material. All these behaviors need to be taken into account to predict material performance during SC growth in polycrystalline materials, which is the aim of this study.

Distribution of microscopic features, such as grain shape/size/orientation, precipitate and flaws within a material, dictates the variability in macroscopic performance, ranging from yield stress to low/high cycle fatigue life. Irwin [17] was the first to point out how fracture toughness depends upon plastic behavior ahead of the crack tip. Subsequently, Rice and Thomson [4] proposed a model that could account for stress relaxation and crack blunting based on dislocation emission at the crack tip. Recent MD simulations [18] of the plastic behavior at the crack tip showed agreement with the theory discussed by Irwin and Rice. Drawing upon these simulations, Argon [19] and Giannattasio and Roberts [20] investigated how the mobility of dislocations is responsible for crack growth and arrest, while George and Michot [13] and Gumbsch et al. [21] studied the relation between crack growth rate and dislocation multiplication at the crack tip in Si single crystals.

Each of the aforementioned microstructure attributes influences SC growth, and, furthermore, engineering materials exhibit a distribution of microstructural features. In order to quantify the variability introduced by the microstructure, we first discuss damage induced during crack growth. Mughrabi [22] related SC growth rate to irreversible plastic strain accumulation during cyclic loading. Consistent with this idea of damage, Bennet and McDowell [23] investigated a nonlocal metric based on the work of Fatemi and Socie [24] that accounts for the importance of the normal stress on the critical slip plane. The Fatemi–Socie parameter was defined as a fatigue indicator parameter (FIP), which has been recently correlated to crack tip displacement by Castelluccio and McDowell [25]. Based on similar analysis, Hochhalter et al. [26] investigated the different possible formulations of FIPs. Their results found a qualitative equivalence of the FIPs in crack behavior, and asserted that FIPs can be used for fatigue life prediction. In this work, we will correlate the variability in FIP parameters in the vicinity of the crack tip to the variability experienced by the ΔK_{th} value in stage 1 of crack propagation. In what follows, we will redefine FIPs as MCDFMs because this name is more general and does not restrict their use to fatigue cycle loading.

The need to address microscopic variability is critical, in order to understand SC growth and ascertain the driving force for crack advancement. The results of this analysis have the potential to more accurately predict fatigue life. Due to the complexity of this topic, many authors in recent years have focused their research on specific microscopic features, in order to provide the foundations for a more complete understanding. But these approaches cannot handle the complex interactions between microstructural attributes. In this paper, we will use a portion of a real microstructure described by a very high-resolution grid to investigate the local influence on variability and show how the change of microstructure parameters influences the behavior ahead of the crack tip. Subsequently, in order to close the loop and to hypothesize a relationship between the variability commonly observed in SC growth rate and the postulated MSCDFMs, we will analyze the behavior of the different microstructure realizations under the effect of different crack lengths. We will also show that the potential crack path is related to extreme values in the MSCDFMs fields and demonstrate that the clustering effect is a crucial parameter in SC behavior.

The paper is organized as follows. In Section 2, we briefly explain the FFT formulation, underlying its key characteristics. In Section 3, we explain the simulations setup, material parameters, and crack geometry. Section 4 is dedicated to the results and discussion: in Section 4.1, we investigate variability in the macroscopic material response; Section 4.2 identifies slip system variability ahead of the crack tip; in Section 4.3, we define MSCDFMs and discuss their correlation with SC behavior; in Section 4.4, we discuss the relation between monotonic and cyclic MSCDFMs behavior, and, finally, in Section 4.5, we discuss the analogy between the variability in the MSCDFMs and SC growth. In Section 5, we draw the conclusions of this study.

2. Model

The elasto-viscoplastic fast Fourier transform-based model (EVP–FFT) developed by Lebensohn et al. [27], is an efficient numerical full-field implementation of the classical crystal plasticity theory [7]. The FFT framework was originally developed by Moulinec and Suquet [28,29] for both linear elastic and nonlinear elasto-plastic composites, and subsequently extended to composites with large mechanical contrast Michel et al. [30,31]. The EVP–FFT model used in this study is the most general formulation of the two previous FFT-based model extensions to polycrystalline deformation in the elastic regime [32] and the rigid-viscoplastic regime [33–36]. The EVP–FFT formulation has been thoroughly described elsewhere, and the readers are referred to [27] for further details. Here we provide a brief overview of the principal characteristics of this method.

Nowadays, very large, high-fidelity 3-D images of polycrystalline microstructures are available and can be obtained with different reconstruction techniques, such as electron backscatter diffraction (EBSD) [37] and synchrotron-based high-energy X-ray diffraction microscopy (HEDM) [38]. The results of these scans are crystallographic attributes, such as grain orientation and phase, arranged in a regularly spaced grid of points (voxels) with subgrain/submicron resolution. One advantage of the EVP–FFT framework, being an image-based technique, is the possibility of directly utilizing these voxelized crystallographic attributes as input of the model, without the need of meshing, as required by finite element methods (FEM). In general, compared with FEM, larger models can be run with the EVP–FFT method due to its computational efficiency (usually between 1 and 2 order of magnitude faster, see [39] for details).

In this methodology, a macroscopic strain is imposed at a certain rate to the unit cell in incremental steps, and the response to this mechanical boundary condition in terms of stress and strain-rate fields is determined. The EVP–FFT algorithm computes a compatible strain field and an equilibrated stress field, which satisfy at every point the constitutive relation. This constitutive relation contains the well-known crystal plasticity rate-sensitive equation. At time $t + \Delta t$, the local elastic relation reads:

$$\boldsymbol{\sigma}(\boldsymbol{x}) = \boldsymbol{C}(\boldsymbol{x}) : \boldsymbol{\varepsilon}^{el}(\boldsymbol{x}) = \boldsymbol{C}(\boldsymbol{x}) : (\boldsymbol{\varepsilon}(\boldsymbol{x}) - \boldsymbol{\varepsilon}^{pl}(\boldsymbol{x})) = \boldsymbol{C}(\boldsymbol{x}) : (\boldsymbol{\varepsilon}(\boldsymbol{x}) - \boldsymbol{\varepsilon}^{pl,t}(\boldsymbol{x}) - \dot{\boldsymbol{\varepsilon}}^{\boldsymbol{pl,t}}\Delta \boldsymbol{t}) \tag{1}$$

where $\boldsymbol{C}(\boldsymbol{x})$ is the forth-order stiffness tensor, $\boldsymbol{\varepsilon}^{pl,t}$ is the plastic strain at time t, and:

$$\dot{\boldsymbol{\varepsilon}}^{pl}(\boldsymbol{x}) = \sum_{\alpha=1}^{N} \boldsymbol{M}^{\alpha}(\boldsymbol{x})\dot{\gamma}^{\alpha}(\boldsymbol{x}) = \dot{\gamma}_0 \sum_{\alpha=1}^{N} \boldsymbol{M}^{\alpha}(\boldsymbol{x}) \left(\frac{|\boldsymbol{M}^{\alpha}(\boldsymbol{x}) : \boldsymbol{\sigma}(\boldsymbol{x})|}{\tau^{\alpha}_{CRSS}(\boldsymbol{x})} \right)^{n} sgn(\boldsymbol{M}^{\alpha}(\boldsymbol{x}) : \boldsymbol{\sigma}(\boldsymbol{x})) \tag{2}$$

where N is the number of slip systems, $\dot{\gamma}^{\alpha}$, $\tau^{\alpha}_{CRSS}(\boldsymbol{x})$ and $\boldsymbol{M}^{\alpha}(\boldsymbol{x})$ are resolved shear strain rate, the critical resolved shear stress (CRSS) and the symmetric Schmid tensor associated with the slip system α, $\dot{\boldsymbol{\varepsilon}}^{pl}(\boldsymbol{x})$ and $\boldsymbol{\sigma}(\boldsymbol{x})$ are the strain-rate and stress tensors at each spatial position, $\dot{\gamma}_0$ is a normalization factor, and n is the rate-sensitivity exponent.

As can be seen from Eq. (2), the plastic flow is governed by the resolved shear stress, which is linked to the stress tensor by the relation

$$\boldsymbol{\tau}^{\alpha}(x) = \boldsymbol{M}^{\alpha}(\boldsymbol{x}) : \boldsymbol{\sigma}(\boldsymbol{x}) = \frac{1}{2}(\boldsymbol{m}^{\alpha}(x) \otimes \boldsymbol{n}^{\alpha}(\boldsymbol{x}) + \boldsymbol{n}^{\alpha}(x) \otimes \boldsymbol{m}^{\alpha}(\boldsymbol{x}) : \boldsymbol{\sigma}(\boldsymbol{x})) \tag{3}$$

where $\boldsymbol{n}^{\alpha}$ is the normal of the slip plane and $\boldsymbol{m}^{\alpha}$ is the slip direction.

The utilization of FFTs comes from the formulation of the micromechanical problem, requiring the determination of the displacement field of a nonlinear heterogeneous medium, which can be calculated as a convolution integral between Green's function of a linear reference homogeneous medium and a polarization field [28,29]. This can be efficiently solved in Fourier space as a simple product, compared to the computationally intensive evaluation of convolution integrals in direct space. Under the FFT-based numerical approach, the micromechanical fields are mapped onto a grid of equally spaced Fourier points (voxels).

Furthermore, the EVP–FT formulation allows for different hardening laws to better describe the material of interest. In this case, a generalized Voce's hardening law [40] is used, as an extension to the one presented by Voce [41]. This hardening law is based on shear strain accumulation on each slip system:

$$\tau^{\alpha}_{CRSS}(\Gamma^{\alpha}_{hard}(\boldsymbol{x}, t)) = \tau_o + (\tau_1 + \theta_1 \Gamma^{\alpha}_{hard}(\boldsymbol{x}, t)) \left[1 - exp\left(-\frac{\Gamma^{\alpha}_{hard}(\boldsymbol{x}, t)}{\tau_1} \right) \right] \tag{4}$$

where τ_0 is the initial CRSS, $\tau_0 + \tau_1$ is the CRSS related to the asymptotic behavior, θ_0 is the stiffness at the end of microscopic linear elastic zone, θ_1 is the asymptotic stiffness at high strain, and $\Gamma^{\alpha}_{hard}(\boldsymbol{x}, t)$ is a weighted sum of the accumulated resolved shear strain of all the slip systems as a function of position, $\boldsymbol{x}$, time, t, slip systems hardening interaction matrix, $h_{\alpha\beta}$ and is given by:

$$\Gamma^{\alpha}_{hard}(\boldsymbol{x}, t) = \sum_{\beta=1}^{N} h_{\alpha\beta} \int_{t=0}^{t} \dot{\gamma}^{\beta}(\boldsymbol{x}) dt \tag{5}$$

In order to complete the crystal plasticity model and to be able to describe lattice rotation the well established multiplicative decomposition of the deformation gradient $F = F^{*} \cdot F^{p}$ (see [7,42]) has been added to the model described in [27]. This operation is performed at the end of each incremental time step Δt in order to maintain computational efficiency. Furthermore this is allowed thanks to the small strain increment assumption.

The authors would like to point out that the presented model does not employ a separate kinematic hardening terms to model the so called Bauschinger effect, also know as back-stress or residual stress, because as shown by Tóth et al. [43], and remarked by Hochhalter et al. [44], early stages of Bauschinger effect are predicted by the polycrystal model itself without additional terms. The modeling strategy employed in the present work is to limit the use of additional terms without experimental data required for a reliable fitting of the additional constants.

As previously discussed, one of the advantages of EVP–FFT is the possibility of direct use of voxelized crystallographic information obtained from 3-D characterization techniques, such as EBSD or HEDM. In contrast to FEM, which can utilize meshes that are conformal to GBs, the use of voxelized information in EVP–FFT introduces stair-stepped GBs. The difference between these two kind of discretizations has been investigated by different authors: (i) Choi et al. [45] performed FEM simulations and pointed out that from a global average point of view the difference is minimal but that plasticity effects can be over/under-estimated in regions close to GBs compared to the case of smooth GBs. In contrast, Pyle et al. [46] and Kanit et al. [47] claimed that stair-stepped grain boundaries gives accurate results and did not show appreciable differences compared to the smooth GBs case (as long as very accurate values of local reorientation are not needed into the analysis). It should also be noted that the FFT algorithm, in contrast to FEM, is a meshless model in which compatibility and equilibrium are imposed to strain and stress fields evaluated at the integration points located in the middle of each voxel, while FEM models impose these conditions at the interfaces between finite elements.

3. Simulation setup and crack design

The microstructure that we use for our analysis is an available 3-D EBSD dataset of a Ni-based superalloy (*IN100*) sample, performed using a dual-beam FIB with a resolution of 0.25 μm [48]. To achieve high resolution, after microstructure reconstruction has been performed utilizing the Dream3D package [49], we extracted a cubic subset of 32^3 voxels from the *IN100* dataset. This subset was subsequently refined to 128^3 voxels, $4 \times 4 \times 4 = 64$ new voxels (with the same orientation) per each voxel in the original image, thus reaching a resolution of 0.0625 μm. The result of the original 32^3 cropping operation and its refinement is a non-periodic unit-cell consisting of an aggregate of 21 grains. The periodic microstructure required by the EVP–FFT model, was obtained by adding a "gas" or "void" phase (infinite compliance, i.e. zero stress), resulting in a cylinder of solid material, as shown in Figs. 1 and 2. This gas phase disconnects the unit cell from its periodic repetitions along the two lateral directions. The assumption of periodicity along the axial direction put in contact the upper and lower surfaces of the cropped image, determining spurious straight grain boundaries, which introduce minor errors (see discussion below).

A limitation of the existing *IN100* dataset is the absence of twin boundaries within the reconstructed microstructure [50]. However, twin boundaries are known to affect the mechanical properties of metals as they effectively reduce the grain size of the structure and provide barriers for dislocation migration, thus influencing the fatigue response of the material [51]. Furthermore, as pointed out by Milligan [52], dislocation looping has not been observed for this material at the temperature 650 °C. Hence, As a first order approximation, we treat the material as homogeneous [53], assuming that the crystals deform

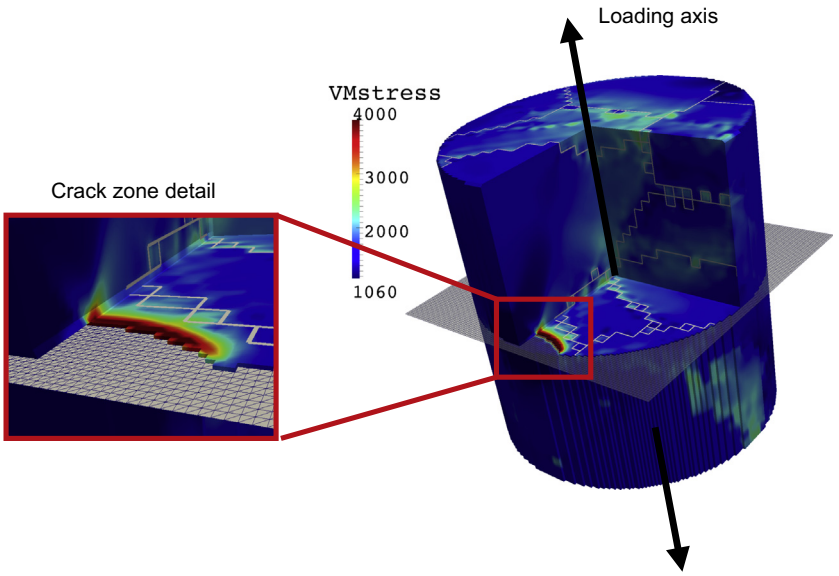

Fig. 1. Overview of the Von Mises equivalent stress distribution. The loading axis and crack are denoted. The shaded plane is the crack plane. Note that this picture has been taken at 0.88% strain.

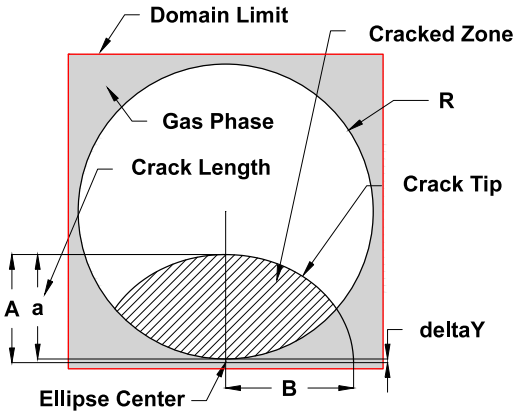

Fig. 2. Sketch of the various crack geometry, illustrating the parameters used to build the crack. Common parameters for all the simulation and realizations are $R = 60$ [Voxel] or 3.75 μm; delta $Y = 1.5$ [Voxel] or 0.094 μm.

plastically by $\{1\,1\,1\}\langle 1\,1\,0\rangle$ octahedral slip, which is the primary mechanism for short crack growth in FCC materials, as pointed out by McEvily and Boettner [2]. To describe the *IN100* elastic behavior, we modeled it as cubic material, e.g. three unique constants describing its elastic response. The single crystal stiffness constants used in this work were obtained from experiments by Shenoy et al. [53]. The Voce hardening parameters were adjusted to represent a uniaxial tensile test, in the 0–10% strain range, obtained at 650 °C, at a strain rate of $8.33 \cdot 10^{-5}\ s^{-1}$ [51]. The hardening response was calibrated for an uncracked microstructure with the loading direction aligned with the longitudinal axis of the cylinder, as shown in Fig. 1. The values of the material parameters utilized for all the simulations are given in Table 1. Furthermore, as specific data to calibrate self and latent hardening coefficient $h_{\alpha\beta}$, was not available, we assumed, as first order approximation, that the slip occurring on each slip system plays the same role in the hardening behavior of the material, in other words $h_{\alpha\beta} = 1$ for all slip systems possible combinations and all the slip systems will harden equally.

We also analyzed the L2 norm of the differences between the Von Mises equivalent stress fields for simulations containing 32^3, 64^3, and 128^3 voxels. The results showed that the difference between simulations containing 64^3 and 128^3 voxels is lower than 5%. Furthermore, we analyzed the effect of the spurious straight grain boundaries normal mentioned above, due to the enforcement of periodicity along the axial direction. As already reported by Rollett et al. [54] we note that a small gradient in the stress field has been introduced in these zones, but it rapidly decreases away from the unit cell limits (2 or 3 voxels in all directions in the most refined grid, depending on the microstructure) and does not interact with the strain fields in our region of interest, near the crack tip.

In our analysis, we are interested in a restricted volume surrounding the crack tip that undergoes much higher values and gradients in both stress and strain fields. In order to capture the influence of microstructure variability at the crack tip, elliptic cracks have been manually inserted in the mid plane of the specimen, by substituting voxels belonging to the material by voxels with void properties (see Fig. 2 for crack geometry details and Table 2 for the crack parameters). Furthermore, in order to observe the variability of MSCDFMs under the effect of different crack length and postulate a relationship between these and the variability observed during SC growth rate, cracks of different length have been manually inserted in different specimens. In this way a quasi-static SC growth can be represented and studied through a collection of multiple simulations with different crack lengths. Moreover, we want to point out that the material history is not retained during different simulations with different crack lengths. This can cause errors in the quantitative evolution of MSCDFMs. However, it should be reminded that the present analysis is qualitative so that trends, not actual values, are of primary interest. It should be noted that the smallest crack (namely the one with length $a = 0.66$ μm) is completely embedded inside a single grain (to be called from now on the *cracked grain*), and the crack grows out of the single grain and becomes transgranular at a length of $a = 1.16$ μm. Also, in order to address variability at the crack tip due to grain reorientation, the *cracked grain* (see Fig. 3) has been randomly oriented in six additional simulations (see the inverse pole figure (IPF) in Fig. 4 for the orientations of the original and six randomly-oriented *cracked grains*). As a result, 35 simulations have been analyzed, corresponding to a combination of seven orientations of the *cracked grain* and five crack lengths.

Furthermore, the boundary conditions utilized in this work are the following for the monotonic loading:

$$S_{imposed} = \begin{bmatrix} 0 & & \\ & 0 & \\ & & \end{bmatrix} \quad E^{max}_{imposed} = \begin{bmatrix} & 0 & 0 \\ 0 & & 0 \\ 0 & 0 & 0.03 \end{bmatrix}$$

where $S_{imposed}$ is the imposed macroscopic stress tensor, $E^{max}_{imposed}$ is the macroscopic strain at maximum load, and only components showing a value have been imposed. For cyclic loading, in addition to the aforementioned condition a strain based cyclic ratio $R_\varepsilon = 0$ has been imposed. The simulation were performed utilizing 4 nodes of the Purdue Conte Cluster which is

Table 1
(a) Elastic and (b) hardening material properties.

Elastic constants (MPa)	Voce's hardening parameters (MPa)
$C11 = 158,860$	$\tau_0 = 485.23$
$C12 = 73,910$	$\tau_1 = 38$
$C44 = 130,150$	$\theta_0 = 1000$
	$\theta_1 = 456$

Table 2
Crack parameters for each crack length, as indicated in Fig. 2.

A Voxel or μm	B Voxel or μm	*a* Voxel or μm
12 or 0.75	20 or 1.25	10.5 or 0.66
16 or 1.00	24 or 1.50	14.5 or 0.91
20 or 1.25	28 or 1.75	18.5 or 1.16
28 or 1.75	36 or 2.25	26.5 or 1.66
44 or 2.75	52 or 3.25	42.5 or 2.66

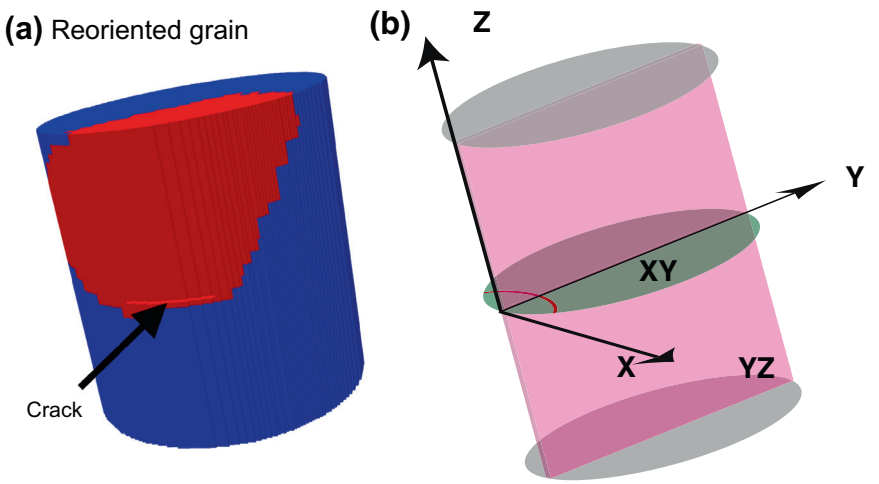

Fig. 3. (a) Shape and position of the *reoriented grain*, in order to note that the smallest crack is completely embedded within the grain. (b) A schematic representing the global reference system: the crack tip (red line), the plane perpendicular to the crack-tip, passing thorough the ellipse center and in the mid point of the crack tip highlighted in pink (named *YZ-plane*), and the crack plane highlighted in green (and named *XY-plane*). (For interpretation of the references to color in this figure legend, the reader is referred to the web version of this article.)

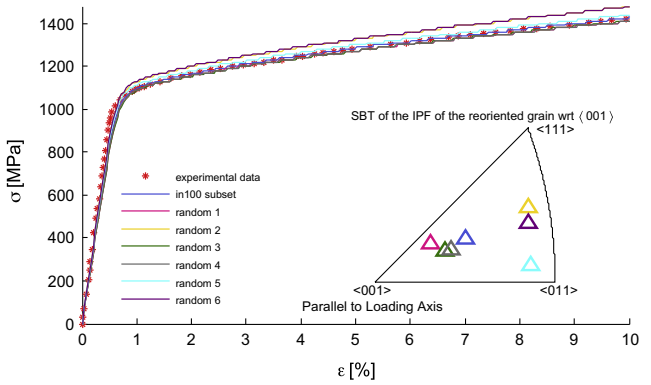

Fig. 4. Macroscopic uniaxial tension (σ_{33} vs. ε_{33}) results of the 7 cracked microstructure realizations and experimental data used for fitting. The variability observed in the macroscopic stress/strain response is due to the fact that the reoriented grain occupies almost 17% of the entire microstructure. Note that the [001] direction is parallel to the loading axis.

equipped with 2 8-core Intel Xeon processors and 64 GB of RAM per node. The cyclic simulation showing a domain of 128^3 integration point ran in less than 4 days. For this specific simulation the bottleneck was due to CPU speed and not to memory requirements.

4. Results and discussion

4.1. Macroscopic variables and local stress field

Before proceeding through the discussion section, we want to point the reader to Fig. 3(b), which identifies a global reference system to be used later on, the *XY-plane* (i.e. the crack plane), and (iii) the *YZ-plane*, which is the plane perpendicular to the crack plane, including the center of the ellipse utilized to generate the crack, and the middle point of the crack-tip.

Fig. 4 shows the macroscopic uniaxial tensile response corresponding to both the experimental data used in the fitting procedure, and the seven different microstructure realizations with a crack length of $a = 0.66$ μm. As it can be seen, the macroscopic behavior is not exactly identical for all realizations. This is due to the fact that the cracked grain, whose orientation is different in each realization, occupies a large volume fraction of the microstructure (see Fig. 3(a)). Differences in both the elastic stiffness and yield stress are observed, although this slightly different macroscopic behavior is not influencing our results, for two reasons: (a) the highest difference in uniaxial stress response for the different realizations at 3% strain is 50 MPa (see Fig. 4), which, if compared with the absolute stress value at this strain, is below 5%; (b) since

we are interested in the variability near the crack tip, the local stress values in this region are dominant compared with the above small deviation. Note also that similar orientations have nearly the same macroscopic response, i.e. the pairs *Random3* (green) and *Random4* (gray) or *Random2* (gold) and *Random6* (purple). Despite this similarity, further investigation of the full Von Mises stress field reveals differences in local behavior, as shown in Figs. 5 and 6. Typically, plotting the stress normal to the crack plane seems like a more natural choice for SC problem, but we choose to plot the Von Mises stress field on 2 different sections of the analyzed realizations. This choice emphasizes the appreciable stress field localization due to microstructure features far away from the crack influence zone and enables the observation of grain clustering.

Figs. 5 and 6 show the equivalent Von Mises stress field of the seven realizations on two different sections, the former corresponds to a section represented by the *XY-plane* (see Fig. 3(b)), and the latter to the section represented by the *YZ-plane* (see Fig. 3(b)). Both figures correspond to 3% macroscopic strain, to emphasize the plastic behavior variability. The lowest value in the color map corresponds to the macroscopic yielding value, $\sigma_y = 1060$ MPa, and the pink ellipses denote some of the major differences between each of the six random realizations and the original one. Also, for brevity, we will designate the deep red zones, which identify highly stressed and plastically deformed areas, as *hot spots* and the deep blue areas, which identify low stress and small plastic deformation zones, as *cold spots*.

Very complex stress fields are found, both in the proximity of the crack tip and near GBs. Microstructural features like GBs represent stress concentrators that are not accounted for in classical elasto-plastic fracture mechanics (EPFM). For this reason, additional insight is needed to capture the complexity of SCG behavior. The multiaxiality of the stress fields resulting form uniaxial loading (at the GBs and at the crack tip) and the anisotropic behavior of the plastic zones found in our simulations are in agreement with the results found by Guilhem et al. [11] and Potirniche et al. [10], respectively.

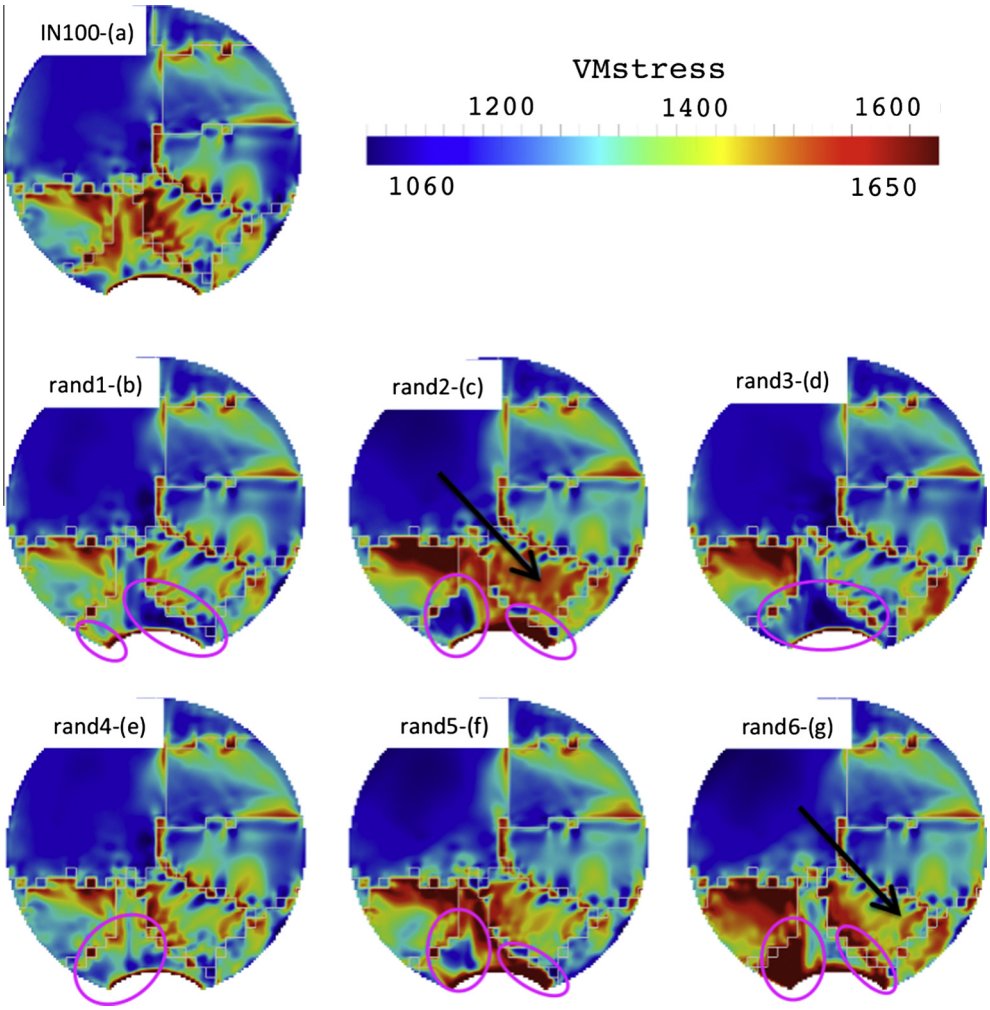

Fig. 5. Comparison of deviatoric Von Mises equivalent stress field on the *XY-plane* (see Fig. 3(b)), for the 7 different microstructure realizations at 3% macroscopic strain: pink ellipse highlight zone with a noticeable difference w.r.t. the stress field shown in subfigure (a). By varying the orientation of the cracked grain, the stress field is modified throughout the polycrystal and not only in the nearest neighbor grains. (For interpretation of the references to colour in this figure legend, the reader is referred to the web version of this article.)

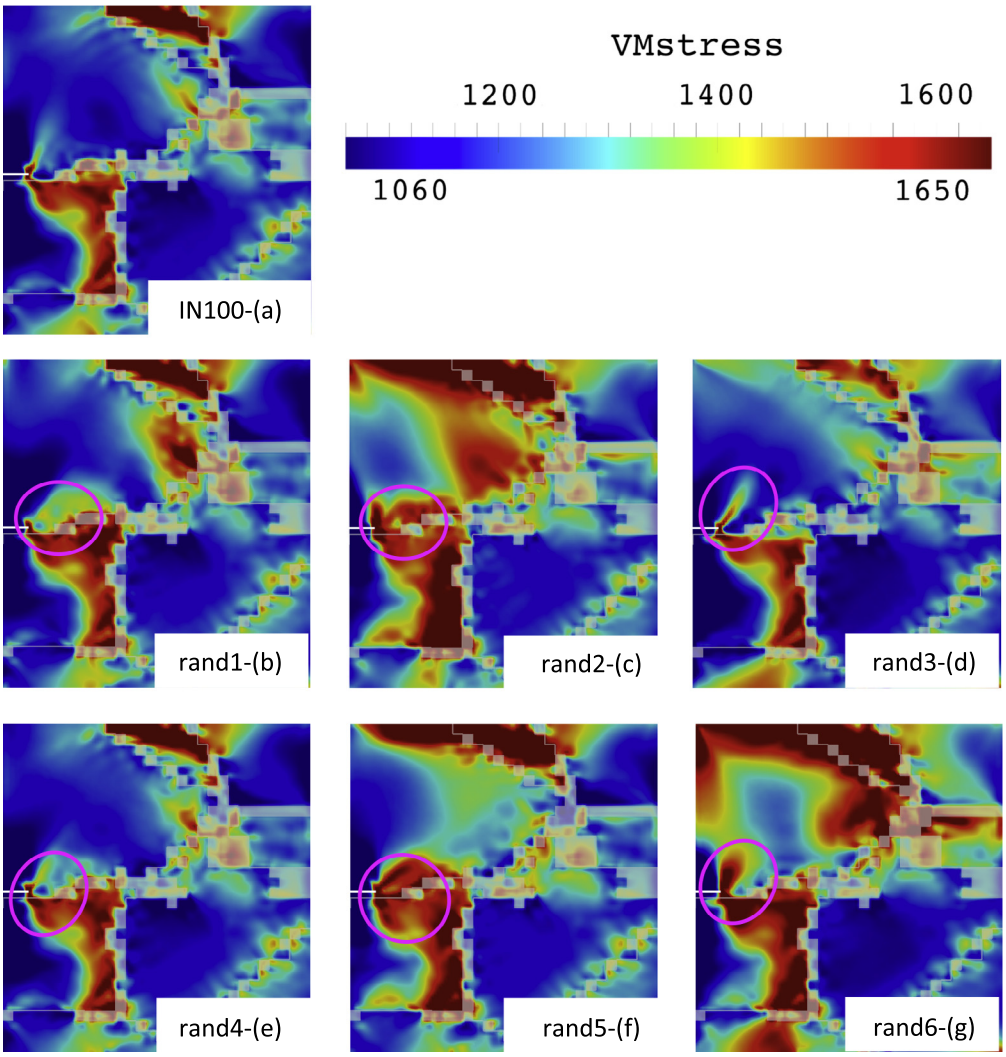

Fig. 6. Similar to Fig. 5, except that here we are looking at the *YZ-plane* (see Fig. 3(b)).

As previously noted, equivalent macroscopic behavior can lead to different local behavior. For example, analyzing the pair of realizations *Random2* and *Random6*, depicted in Fig. 5(c) and (g), respectively, we can immediately recognize variability ahead of the crack tip. In fact, the hot and cold spots show a complete opposite behavior in these two realizations, despite their similar orientation (see Fig. 4). In Fig. 5(c), we can identify a cold spot on the left, just ahead of the crack tip, and a hot spot on the right, which interacts with the GB structure just in front of the crack tip, extending until the next GB. In Fig. 5(g), hot spots are located on adjacent sides of the GB, thereby creating a link between the stress induced by the crack tip and GB structure, which suggests a possible crack path. Furthermore, this variability influences the stress distribution in the neighboring grain. Regarding two other realizations, *Random3* and *Random4*, depicted in Figs. 5(d) and (e), respectively, we note that, despite the similarities in the *cracked grain* orientation and the corresponding stress fields, the average level of the von Mises stress ahead of the crack tip shows a variability of around 200 MPa. In both cases, the differences in the hot/cold spots extension and position suggest that the crack may grow at different rates in different directions due to the presence of GBs [10] and misorientation between neighboring grains [8,9]. Furthermore, the different behavior experienced by neighbor grains indicates the need to analyze clusters of grains, as pointed out by Guilhem et al. [11]and Sangid et al. [12] in the context of a microstructure-sensitive SCG theory.

As first pointed out by McEvily and Boettner [2], dislocations are emitted in an orderly manner from the crack tip on highly stressed slip planes. By inspecting the variability in Fig. 6, we note the difference in the angles, extension, and shape of the lobes of hot spots surrounding the crack tip and their wake. The difference in angle of the hot spot lobes between the various realizations is a clear indication of the influence of grain orientation at the crack tip. Meanwhile, asymmetry of these hot spot lobes contains information about neighboring grain misorientation and distance. It should be noted that a GB is

present just beneath the crack, leading to high stresses in this direction. Moreover, not all the realizations show the same hot spots in this area. For instance, *Random3* and *Random5,* depicted in Fig. 6(d) and (f), respectively, have a branch of the hot spot distribution following the GB direction; while *Random6,* depicted in Fig. 6(g), has a very bulky hot spot following the GB and extending very deeply into the neighbor grain. Furthermore, in other realizations, such as *IN100*, *Random1*, and *Random4* (Fig. 6(a), (b) and (e), respectively), we can observe the hot spot below the crack tip, after passing through the GB, follows a well-defined orientation imposed by the slip plane of the neighboring grain.

By analyzing the hot spots in the *cracked grain*, we observe that the *IN100* and *Random4* realizations (see Fig. 6(a) and (e), respectively) show a very limited hot spot at the crack tip, with a large plastic zone at a lower stress level. Meanwhile, *Random3* (see Fig. 6(d)) has a long hot spot with a well-defined direction and a very tight wake, and *Random6* (see Fig. 6(g)) shares the same well defined behavior of *Random3,* but with much thicker hot spots and wake areas. *Random3* has hot spots nearly oriented in the load direction, with one of them bridging towards the highly stress zone at the crack tip, interacting with another one, at the GB. *Random5* has three hot spots departing from the crack tip in three well-defined directions. Additionally, we note that the fields predicted at lower strains show that plasticity starts to play a role even when the global behavior is still in the linear elastic zone, and that the shape of plasticized areas at lower strains are consistent with the ones shown in Figs. 5 and 6. Furthermore in some cases, hot spots are found not at the crack tip, but in its vicinity just passed the GB, displaying the effects of stress anisotropy between grains.

We can briefly explain this behavior from a dislocations dynamics point of view. Smaller hot spots areas in both Figs. 5 and 6 are consistent with emission of edge dislocations at the crack tip on highly stressed slip planes, which have the property to relax stresses by blunting the crack and, in turn, diminishing the avalanche mechanics of dislocation emission [14]. In general, the hot spots and preferred sites for dislocation emission could be in place only in a portion of the crack tip surface, thus explaining differences in behavior amongst the different spatial locations and realizations, enhancing variability. GBs act as both dislocation sources and energy barriers to incoming dislocations [16], creating local hot spots ahead of the crack tip in the bulk of the material. A bridging effect between hot spots is observed between the GBs towards the crack tip, and vice versa. This phenomenon does not always follow the primary hot spots orientation, suggesting that more than one slip plane has been activated, e.g. Fig. 6(c). Furthermore, according to Lee et al. [55], the interaction between dislocations and GBs can have 3 major consequences: (i) cross-slip into adjacent grain, (ii) partial transmission, resulting in residual dislocations incorporated in the grain boundary, (iii) dislocation blocked at GBs. Eventually, mechanisms (ii) and (iii) can lead to impeded dislocation motions [12], subsequently preventing further dislocation emission.

4.2. Slip system activity

To achieve a better insight on the variability at the crack tip, a statistical analysis of the resolved shear stress has been performed on the crack plane. Fig. 7(a) shows the volume fraction of active slip systems as a function of resolved shear stress, for the seven different realizations with a crack length $a = 0.66$ μm at 3% strain, over the volume schematically represented by grey dots (as shown in the inset within Fig. 7(a)), where each dot represents a voxel. The dash-dotted vertical lines represent the maximum and the minimum value of the averaged resolved shear stress at the crack tip (represented by black stars), while dashed vertical lines represent the same quantity, four voxels ahead of the crack tip (represented by red stars). Fig. 7(b) depicts the cumulative volume fraction of active slip systems ahead of the crack tip (same volume analyzed in Fig. 7(a)) versus the resolved shear stress level. The first thing that should be noted in Fig. 7(a) is that the curves are not of equal area, as can be clearly seen in Fig. 7(b), meaning that a different number of slip systems are activated in different realizations. Recently, Zhang and Ghosh [15] investigated the relationship between grain orientation and dislocations emission on a pre-cracked Ni single crystal through MD simulations, finding a variability in both type and number of dislocations, depending on the orientation. These dislocations subsequently interact with each other in different ways, leading to completely different material performance. This same behavior is observed in our simulations at the scale of the microstructure.

Furthermore, other parameters underlying the variability in material behavior at the crack tip can be noted. The values of the resolved shear stress at the peaks of the PDF are consistent with the location of the average resolved shear stress, four voxels ahead of the crack tip. The maximum spatial average of the RSS four voxels away from the crack tip is observed in *Random6* with a value of 655.2 MPa, while the minimum is observed in *Random2* with a value of 530.8 MPa. This corresponds to an average RSS range of 124.4 MPa. By changing the analyzed volume and moving closer to the crack tip, more variability is seen in the averaged resolved shear stress, e.g. the maximum spatial average of the RSS is observed in *Random6* with a value of 955.8 MPa, the minimum of the same quantity is observed in *Random3* with a value of 607.2 MPa, corresponding to a range of 348.6 MPa. In other words, moving away from the crack tip, the average value of the resolved shear stress is less influenced by the presence of the crack, thus becoming more homogenous. Also, the volume fraction at which peaks are found undergoes a high variability, going from 6% in *Random4* to more than 13% in *Random5*. Analyzing comparable realizations, like the pair *Random3* and *Random4* (see Fig. 4), the variability in behavior is evident by analyzing the tail lengths, peak positions and volume fractions. A similar variability can be seen in similar pair, *Random2* and *Random6*, by looking at the average value of the resolved shear stress four voxels away from the crack tip, of which these realizations represent the two extreme values. These results emphasize the need of accounting for this variability in slip activity, as it has direct implications on the crack driving force (the reader is referred back to Fig. 4 to identify grain orientation).

In the context of FFT-based calculations, Moulinec and Sequet [56] and Rollett et al. [54] pointed out that the variability observed in the length of the tail of the strain rate probability density function is related to strain localization, which in turn

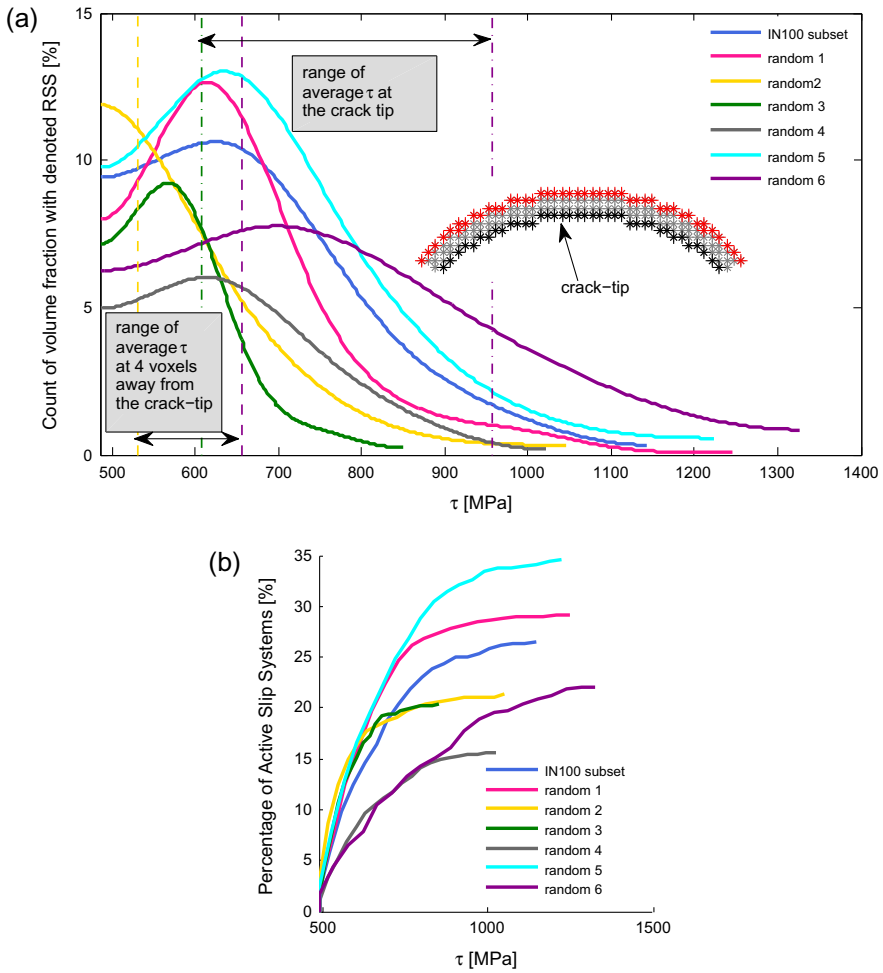

Fig. 7. (a) Volume fraction of active slip systems w.r.t. resolved shear stress in the first 4 rows of voxels in front of the crack tip, within the crack plane (see figure). It should be noted that this curves are not equal area and start from critical resolved shear stress (after binning process, the data have been interpolated utilizing natural splines). In the case when the macroscopic results are almost the same (i.e. *Random2* and *Random6* realizations), their distributions and peak positions vary significantly; (b) Cumulative volume fraction of active slip systems versus resolved shear stress in the first 4 rows of voxels in front of the crack tip, within the crack plane (see (a)): a very heterogeneous slip activity is present in the analyzed voxels. Moreover the number of active slip system is not only related to the orientation of the cracked grain: i.e. *Random3* and *Random4* realizations, that are really close in the IPF figure, has a substantial difference in the count of active slip systems.

correlates with favorable slip planes for crack growth, as pointed out by McEvily and Boettner [2]. If one assumes the crack growth rate follows the model of slip process proposed by Neumann [3], then it follows that the variability observed in the tail length of the probability density function of the resolved shear stress could be related to the variability of the short crack growth rate, because this phenomenon is governed by extreme values of the resolved shear stress fields.

From a SC behavior point of view, variability needs to be addressed. As we move closer to the crack tip, its effect becomes more and more dominant (see range of average resolved shear stress in Fig. 7(a)), due to crystallographic features that play a crucial role in dislocations emission and evolution, which in turn influence growth rate. It should also be noted that these findings, especially the total percentage of active slip systems, suggest localized activity in highly stressed slip planes, which can lead to localized damage. Sadananda and Glinka [57] pointed out the direct dependence of SC advancement from dislocation emission at the crack tip. In particular, they showed how the interaction between dislocations, microstructure and flaws can lead to very complex dislocations arrangements, due to different mechanisms, like activation of different slip systems, cutting of dislocations, annihilation of edge dislocations producing vacancies, cross-slip of screw dislocations, shearing of particles, presence of GBs, etc. All these mechanisms can lead to slip irreversibility, which increases the SC growth rate [22]. The complex scenario shown in this section emphasizes the critical role of slip irreversibility as directly influenced by the variability of the microstructure, due to different slip system activity. This entails different cyclic damage accumulation, which in turn leads to variable SCG rate, influencing macroscopic performance.

4.3. Damage quantification

At this point, it is pertinent to quantify damage accumulation. As stated by Mughrabi [22], damage accumulation can occur in both the surface and bulk of fatigued metals. Recently, the fatigue research community has adopted different Fatigue Indicator Parameters, which as already mentioned, we call Microstructural Short Crack Driving Force Metrics (MSCDFMs), to quantify damage accumulation even for monotonic load conditions. For instance, Hochhalter et al. [26] identified five different MSCDFMs, three of which are based on accumulated plastic resolved shear strain, one is based on maximum energy dissipation, and the last one is based on the Fatemi–Socie parameter. The work of Fatemi and Socie [24] focused on multi-axial fatigue, and emphasized the role of normal tensile stress on the critical plane, following the work of Brown and Miller [58]. At the microscale level, the importance of the critical plane in multi-axial fatigue has also been investigated by Bennett and McDowell [23], and recently confirmed by Tschopp and McDowell [59] using MD simulations to show that a tensile normal stress on the slip plane considerably lowers the shear stress required to nucleate a dislocation loop. In our work, we will use three of the five MSCDFMs analyzed by Hochhalter et al. [26], maintaining the same notation for sake of consistency:

$$\mathrm{D1}(x) = \max_{\alpha} |\Gamma^{\alpha}(x)| \tag{6}$$

$$\mathrm{D3}(x) = \sum_{\alpha=1}^{N} |\Gamma^{\alpha}(x)| \tag{7}$$

$$\mathrm{D5}(x) = \max_{p} \sum_{\alpha=1}^{N_s} |\Gamma_p^{\alpha}(x)| \left(1 + k \frac{\langle \sigma_n^p(x) \rangle}{\tau_0(x)}\right) \tag{8}$$

where Γ^{α} is the accumulated plastic resolved shear strain on the selected slip system, N is the total number of slip systems, p identify the slip plane, $\langle \sigma_n^p \rangle$ is the tensile stress acting on the slip plane p ($\langle \cdot \rangle$ are the Macaulay brackets defined such that $\langle x \rangle = 0$ if $x \leqslant 0$ and $\langle x \rangle = x$ if $x > 0$), k is the weighting factor dictating the importance of tensile stress with respect to plastic slip, that has been set to 0.5 as suggested by Fatemi and Socie (1988), and N_s is the number of slip-system present in the pth slip plane. Eq. (6) identifies the slip system with the maximum accumulated plastic resolved shear-strain. Eq. (7) represents the total accumulated plastic resolved shear-strain in each voxel. Eq. (8) represents the maximum accumulated plastic shear strain amongst planes subjected to tensile normal stresses. It should be noted that in the literature these MSCDFMs have been used to quantify the slip irreversibility at the end of a fatigue cycle, (e.g. [25]). Within our EVP-FFT framework, we limit our analysis to monotonic loading with an applied stress ratio, $R = 0$, thereby limiting our possible sources of slip irreversibility, but still identifying hot spots in the microstructure as potential sites for slip irreversibility.

Additionally, we investigated three MSCDFMs based on energy dissipation [60] that have been formulated as follows:

$$\mathrm{E1}(x) = \max_{\alpha} |\Gamma^{\alpha}(x)\tau^{\alpha}(x)| \tag{9}$$

$$\mathrm{E3}(x) = \sum_{\alpha=1}^{N} |\Gamma^{\alpha}(x)\tau^{\alpha}(x)| \tag{10}$$

$$\mathrm{E5}(x) = \max_{p} \sum_{\alpha=1}^{N_s} |\Gamma_p^{\alpha}(x)\tau_p^{\alpha}(x)| \left(1 + k \frac{\langle \sigma_n^p(x) \rangle}{\tau_0(x)}\right) \tag{11}$$

Eqs. (9)–(11) are the energetic equivalents of D1, D3, and D5, respectively. Moreover, we describe a reference system that will be used throughout the following discussion. Fig. 8(a) and (b) shows respectively, θ the angle of maximum MSCDFMs direction on the *YZ-plane* (see Fig. 3(b)), and φ, the angle of maximum MSCDFMs position at the crack tip on the *XY-plane* (see Fig. 3(b)).

Fig. 9 shows the contour plots on the *YZ-plane* (see Fig. 3(b)), of all six different MSCDFMs (Eqs. (6)–(11)), at a macroscopic strain $\varepsilon_{33} = 0.32\%$. It should be noted that at this strain level, the direction of maximum MSCDFM, namely θ, is around ±90°, due to the lack of plasticity developed near the crack tip at this low applied strain level (see Fig. 4). Additionally, the plastic

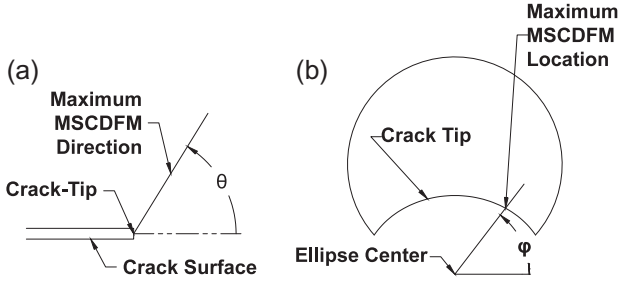

Fig. 8. Schematic of maximum MSCDFM angle reference (a) in *YZ-plane* (see Fig. 3(b)) and (b) in the *XY-plane* (see Fig. 3(b)).

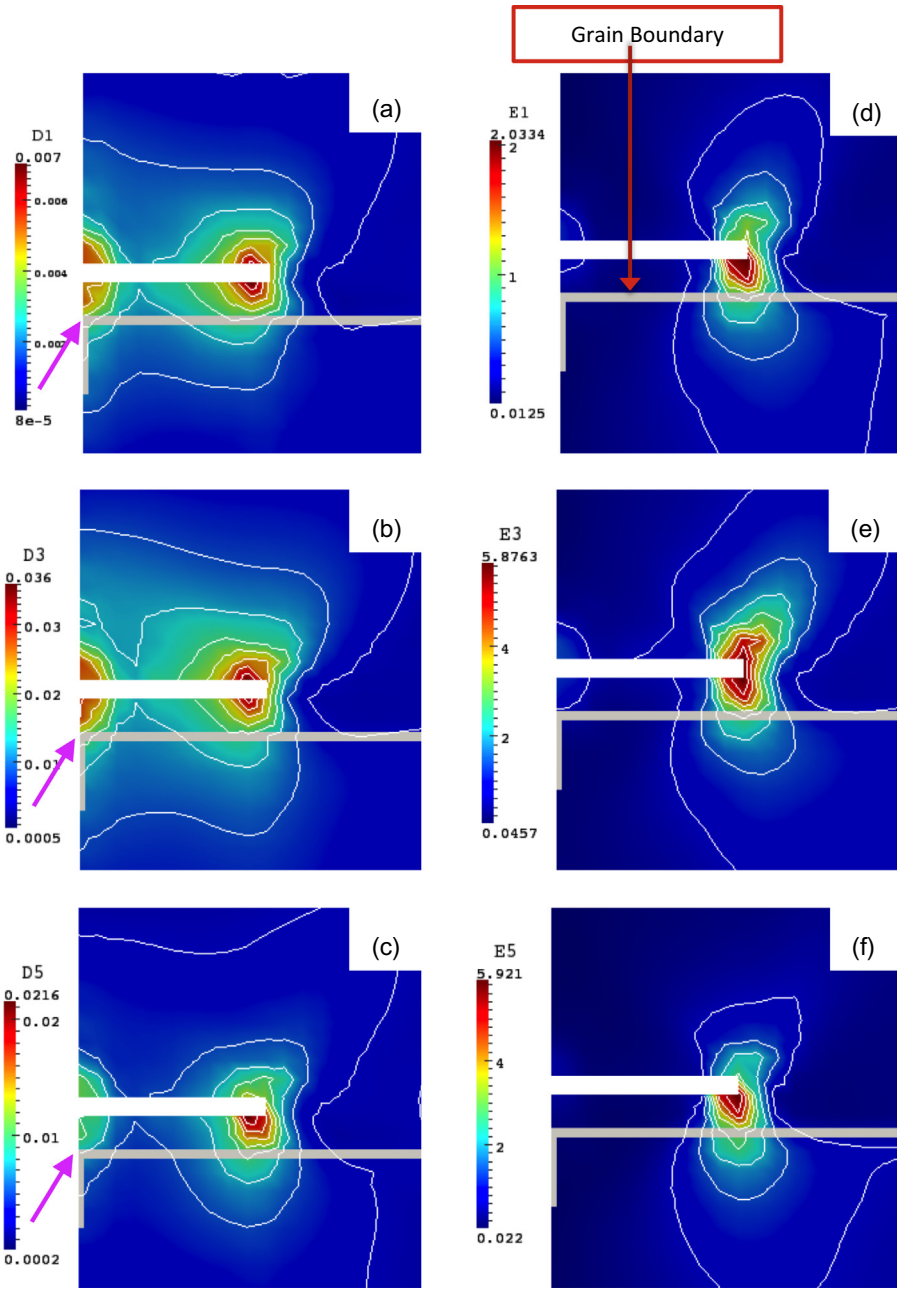

Fig. 9. Different MSCDFMs field comparison on the *YZ-plane* (see Fig. 3(b)) at the crack tip of the IN100 subset, at low strain $\varepsilon_{33} = 0.32\%$ (almost in the middle of the linear elastic region as shown in Fig. 4). It should be noted that at this strain, the direction of maximum MSCDFM is around ±90° this is due to the fact that, at this strain, plasticity is not well developed. Furthermore it should be noted that even at low strain the shape of this 6 indicators are very different, also the 3 energetic indicators seems to be more sensitive microstructure features like Grain Boundaries.

strain-based MSCDFMs, D1, D3, and D5, have a very similar behavior and shape, as pointed out by Hochhalter et al. [26], while the energetically-based MSCDFMs, E1, E3, and E5, are much more sensitive to crystallographic features, as can be seen in Fig. 9(d)–(f). The shear-based MSCDFMs show 2 anomalies in the location of hot spots: (i) the first maxima highlighted in pink in Fig. 9(a–c) is due to numerical artifact caused by the presence of voxels of different orientation at the interface between solid and gas phase (see pink arrow) and to the higher compliance at the crack flanks; (ii) the maxima that should be located at the crack tip, are at a spatial location a voxel behind the tip, this unexpected effect is probably due to interaction of the stress fields caused by the crack tip and the one generated from the grain boundary just beneath it. In contrast we note the energetic MSCDFMs, E1, E3, and E5, display their maximum value just ahead of the crack tip, which is the expected location for maximum damage for a fatigue crack. The complete MSCDFMs evolution for the *IN100* realization is shown in

Video #1, which is available as a supplement to this paper. Due to some of the E5 MSCDFM field features, such as maximum damage at the crack tip, sensitivity to microstructure features, and other motivations that will be pointed out in next section, we postulate E5 as the best candidate to explain a possible crack path; thus the E5 MSCDFM is used exclusively in the contour plots within the rest of this section.

Fig. 10 shows the contours plot for the seven different realizations with a crack length $a = 0.66$ μm at a strain $\varepsilon_{33} = 3\%$. Substantial differences can be observed in the maximum value of the E5 MSCDFM, between the different realizations. For instance *Random6*, which is depicted in Fig. 10(g), shows the widest hot spot area, in contrast to *Random2* (Fig. 10(c)), which has the minimum value of the E5 MSCDFM. Furthermore, variability can be noted in the relative location of the hot spot with respect to the crack tip, e.g. the former is located near the crack tip, while the latter denotes subsurface damage (see black arrow in Fig. 10(c)). The variability in the E5 MSCDFM fields is distinct between these realizations, *Random2* and *Random6*, albeit the corresponding *cracked grains* have similar orientations, as denoted by their position in the IPF (see Fig. 4). This behavior is most likely an effect of grain clustering combined with the fact that a single IPF figure cannot fully represent

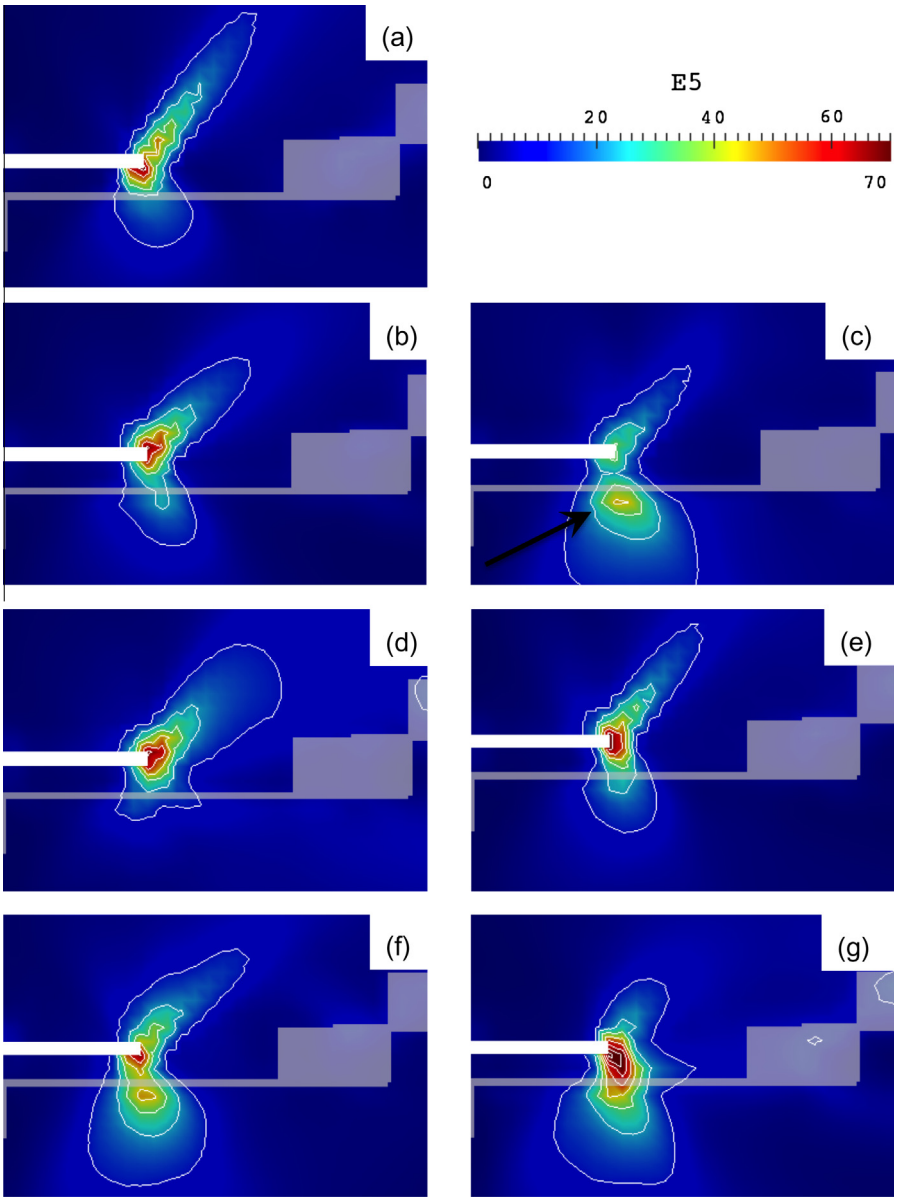

Fig. 10. Comparison of MSCDFM E5 field on the *YZ-plane* (see Fig. 3(b)) in all microstructure realizations (different orientation of the cracked grain). As can be noted from the images the shape, orientation and even the maximum values of E5 change a lot suggesting a very complex local behavior. The different behaviors suggest a complex slip activity ahead and near the crack tip, such that, the angle at which lobes of damage material advance change with the orientation. Furthermore sub-surface damage accumulation can be related to crack deviation and bifurcation.

an orientation, i.e. more than one IPF is needed to completely represent a grain orientation. By viewing another pair of similar orientations of the *cracked grain* (*Random3* and *Random4* in Fig. 10(d) and (e)), the former shows grain shielding with a positive angle θ, while the latter shows nearly a symmetric profile, e.g. two lobes in two different directions, each containing almost the same MSCDFM values. Therefore, the orientation of the cracked grain is not a sufficient condition to identify SCG behavior.

The damage accumulation can be correlated with different physical phenomena, for instance as the crack tip is near a GB, we can observe sudden changes in crack-direction [26]. This is attributed to the irreversibility of slip near the GB. When a dislocation impinges upon a GB, in most cases due to strain incompatibility, a residual dislocation is formed within the GB, which is often a source of slip irreversibility in cyclic loading [16]. As damage in the form of slip accumulates at the GB and the GB is saturated with defect density, the crack can either propagate in the direction of the GB leading to intergranular fracture, or continue along slip planes resulting in transgranular fracture. Grain shielding is an effect due to GBs that impede dislocation motion or dislocation entanglement between the crack tip and the GB. In the case of transgranular fracture, dislocation motion will follow the minimum energy principle, as dislocation dynamics inside the grain will occur where the resistance to slip is lowest. This could be achieved for a high misorientation between all the slip planes in the adjacent grains, while grain shielding is due to a dislocation pile-up at the GB that, in turn, will generate a high stress field impeding further dislocation motion relative to the field. As shown in Fig. 10, many of the contour plots of the E5 MSCDFMs traverse the GB that is located directly below the crack. For a better understating of the E5 MSCDFM evolution with various microstructure realizations, we invite the reader to watch Video #2.

Fig. 11 shows the 3D iso-surfaces of $E5 = 25\ \mathrm{Jm}^{-3}$ of four different realizations, namely (*IN100*, *Random2*, *Random3* and *Random5*) at global strain $\varepsilon_{33} = 0.76\%$, for a crack length of $a = 0.66\ \mu\mathrm{m}$. It can be seen that the variation in microstructure produces different shapes and features of these iso-surfaces, where the colors are coherent with those shown in the symbols within the IPF (Fig. 4). The realization denoted *Random3* has the smallest surface, indicating less damage accumulation surrounding the crack compared to the other realizations. We invite the reader to visualize the evolution of these iso-surfaces in Video #3 in the online Appendix.

Fig. 12 shows the behavior of MSCDFM E5, depicting different contour plots for the *IN100* realizations at different crack length (Table 2), for a macroscopic strain $\varepsilon_{33} = 3\%$. As expected, the maximum value of E5 is increasing with increasing crack length, as shown by the increasing area of the damaged region, and the contours within the region of the E5 MSCDFM fields. The shape of the damaged region is not distinctively different until the crack reaches a microstructural feature (e.g. adjacent GB), namely until $a = 1.16\ \mu\mathrm{m}$. As can be seen in Fig. 12(d), the damaged zone branches or bifurcates in the direction of the GB, as the stress fields associated with the crack interact with the elevated stress fields due to the presence of GBs. It should be noted that the range of E5 MSCDFMs undergoes substantial variability with respect to the length of the crack (more than two orders of magnitude increase in maximum MSCDFM value with respect to crack length).

In order to have a better insight on the behavior of the different postulated MSCDFMs, we pick a representative candidate (realization *Random5*, crack length $a = 0.66\ \mu\mathrm{m}$, global strain $\varepsilon_{33} = 1.04\%$) for further analysis. Fig. 13(a) shows the location of the maximum MSCDFMs (D1, D3, D5, E1, E3, and E5) relative to the profile of the crack tip and the ellipse center (red star). In this case, the locations of maximum MSCDFM values coalesce at the same position, but in general the maximum MSCDFM values do not necessarily occur in the same location. Fig. 13(b) indicates the values of the normalized MSCDFMs (w.r.t. their own maximum value along the analyzed path) vs. distance from the crack tip along the direction given by angle φ (see Fig. 8(b)). Fig. 13(c) shows: (i) the spatial line representing the directions of maximum MSCDFM integral (solid colored lines), (ii) the projection of the principal stress axes (blue dashed lines), (iii) the projection of the slip planes (dashed-dotted black lines) on *YZ-plane* (see Fig. 3(b)). It can be seen that the directions of maximum MSCDFMs integral are not the same, and, except in seldom cases, they are not aligned with slip planes. Finally, Fig. 13(d) displays the maximum value of the normalized MSCDFM along the direction referenced by the angle θ (Fig. 8(a)). The variability observed in both the location of the maxima along the crack tip and the angle representing the line with the maximum MSCDFM's integral, and of course

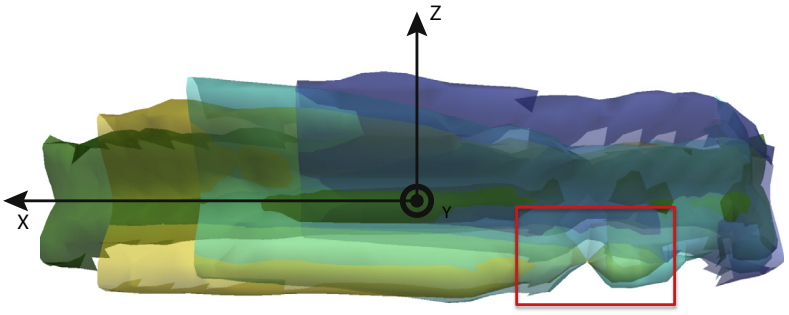

Fig. 11. Iso-surfaces at the crack tip (see Fig. 3(b) for the reference system) of MSCDFM E5, colors are coherent with IPF. It should be noted the differences in shape and size, while some microstructure features are in common i.e. hot/cold spots for some realizations (see highlighted zone in the figure). (For interpretation of the references to colour in this figure legend, the reader is referred to the web version of this article.)

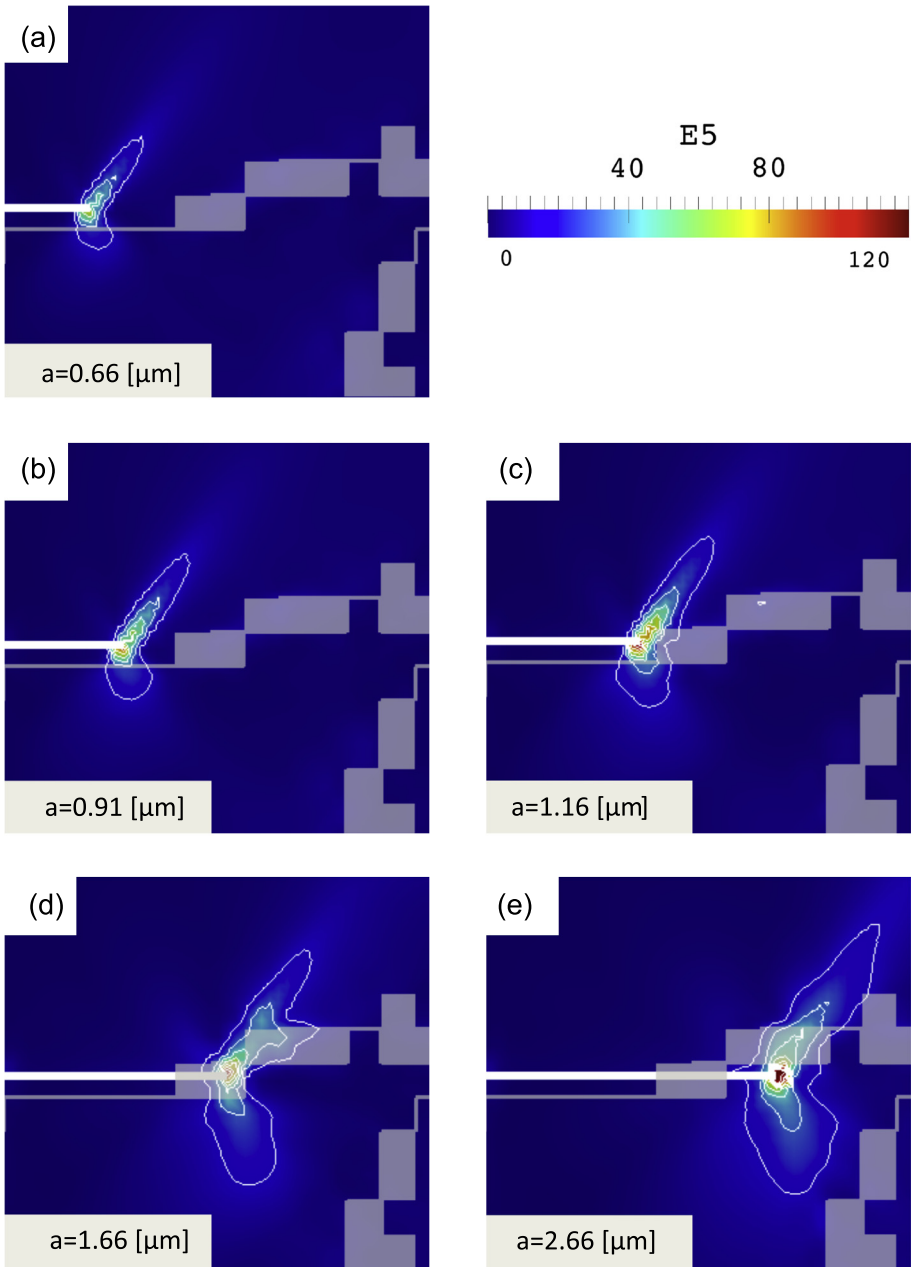

Fig. 12. Comparison of E5 on the *YZ-plane* (see Fig. 3(b)) in *IN100* subset at different crack lengths. In this figure, by increasing the crack lengths, as the crack moves towards more complex microscopic features, i.e. grain boundaries, the shapes of the MSCDFM iso-surfaces change very significantly. At a = 1.66 μm we can see how the iso-surfaces is following the GBs away from the crack tip; compared with a = 2.66 μm, the iso-surfaces seem to through GBs almost without being affected.

their values, can be related with the variability observed in the SC growth rate (this specific topic will be discussed in Section 4.5)

As discussed by McEvily and Boettner [2], Brown and Miller [58], Fatemi and Socie [24], and Bennett and McDowell [23], the critical plane plays a significant role in fatigue behavior. In order to elucidate its role, we compared the alignment of Maximum MSCDFMs integral's path with: (i) the slip planes in the microstructure, and (ii) the principal stress axes during loading (see Figs. 8(a) and 13(c)). Fig. 14(a) shows the average misalignment, given by,

$$\overline{\Delta\theta_i} = \frac{\sum_{q=1}^{Nsim} \Delta\theta_i^q}{Nsim} \tag{12}$$

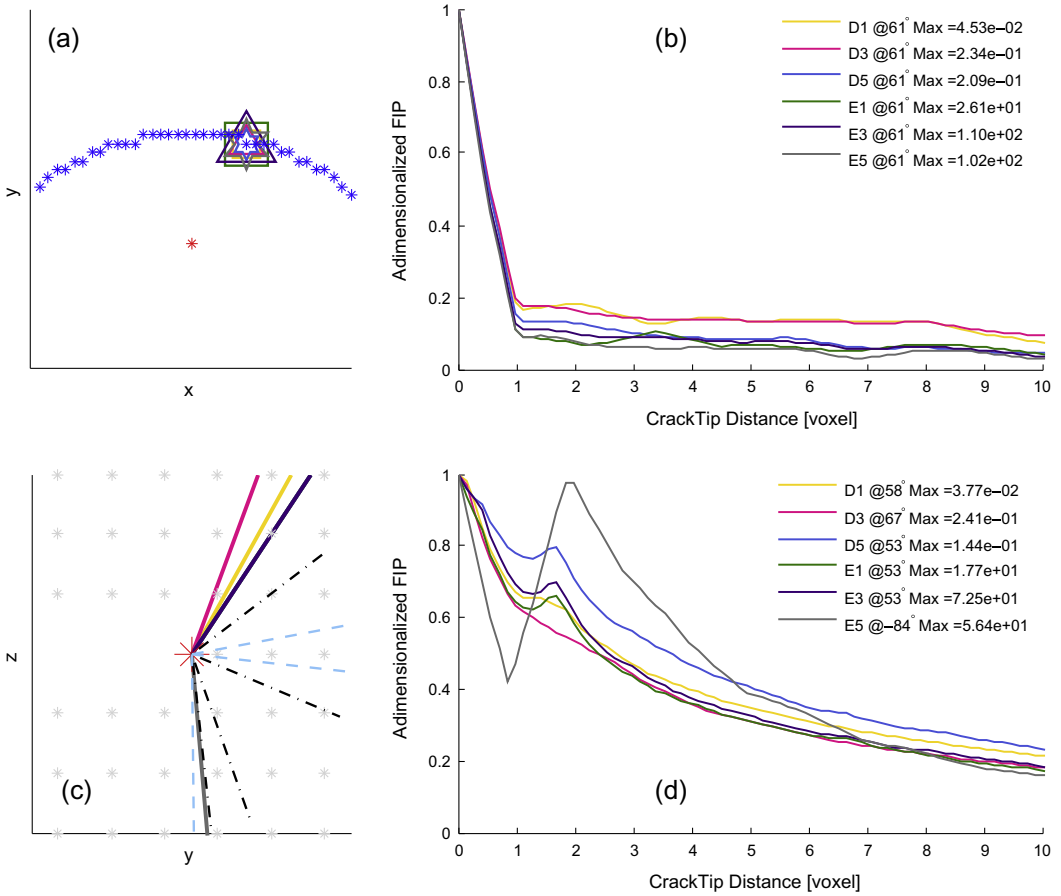

Fig. 13. This particular case represents the subsurface damage (see Fig. 10 realization *Random5*). (a) The spatial line relatively to the *XY-plane* (see Fig. 3(b)) in which the MSCDFM has been evaluated, blue dots represent the crack tip, red dot, the center of the ellipse, and symbols on the crack tip, the location of the maximum MSCDFM at the crack-tip. (b) The values of nondimensionalized MSCDFM with respect of its maximum vs. crack tip distance, in this case their values drop very rapidly going away from the tip in the crack plane. (c) The spatial line relative to *YZ-plane* (see Fig. 3(b)) indicating the maximum MSCDFM angle, black dashed line represent the projection of the 4 slip planes in the middle section of the ellipse, normal to the crack plane, and blue lines represent principal stress axis. It can be seen how some MSCDFMs are aligned with slip planes like E5 in this particular case. (d) Along the spatial line in (c) the value of the each MSCDFM is plotted along its maximum direction. The maximum value as not always located at the crack-tip, but can be ahead of the crack. (For interpretation of the references to colour iny this figure legend, the reader is referred to the web version of this article.)

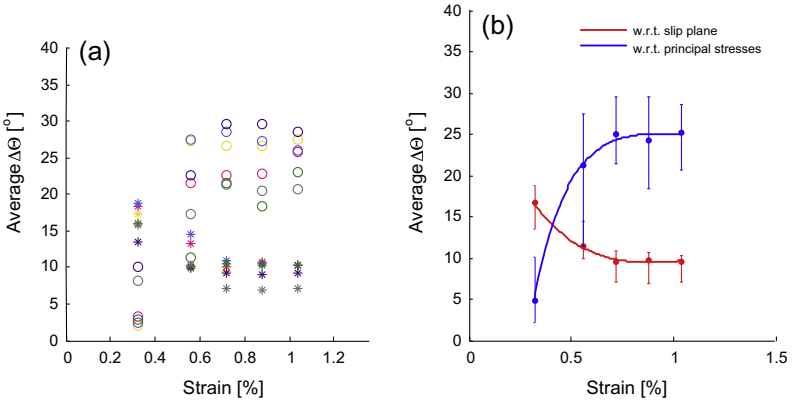

Fig. 14. (a) Alignment between the spatial line trace of the maximum MSCDFM to that of the slip planes (indicated by stars) and principal stresses axes (indicated by circle), as function of the macroscopic strain for a fixed crack length of $a = 0.91$ μm (b) trend of diminishing distance between MSCDFM and slip plane, and increasing between MSCDFM and principal stress axes is shown, where error bar represents the minimum and maximum variation.

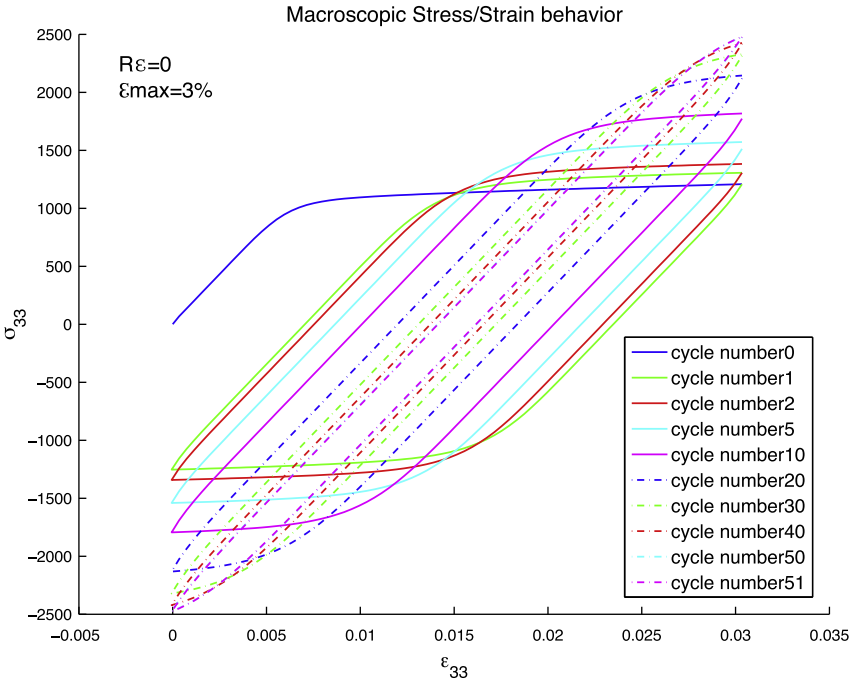

Fig. 15. Macroscopic stress vs. strain behavior of the *IN100* realization with a crack length of 0.91 μm: $\varepsilon_{max} = 3\%$, $R_\varepsilon = 0$.

where *Nsim* is the number of different realizations (7), *i* identifies the MSCDFM, and $\Delta\vartheta$ is the minimum absolute value of the misalignment between the MSCDFM maximum direction angle and the adjacent slip-plane/principal stress axis, at different strain levels. Fig. 14(b) shows the trend lines of Fig. 14(a) with error bars representing MSCDFMs variability, and dots representing the average misalignment of all MSCDFMs i.e.

$$\overline{\overline{\Delta\theta}} = \frac{\sum_{i=1}^{N^{MSCDFMs}} \overline{\Delta\theta_i}}{N^{MSCDFMs}} \tag{13}$$

where $N^{MSCDFMs}$ is the number of different MSCDFMs investigated (6), at each strain level. It should be noted that the misalignment between the slip planes and MSCDFMs decreases, while the misalignment with principal stress axis increases. This behavior is due to the fact that at small strains, plasticity has just started to develop and unevenly distributed damage starts to appear in the proximity of the crack tip, while the majority of the material is still in the elastic regime, which is governed by principal stress axes. This behavior is consistent with our choice of E5 as the most pertinent MSCDFM. Additionally, the misalignment of the MSCDFM and slip planes with increasing strain may be due to two different mechanisms. One of them is grain rotation near the crack tip, which, in the present cases of low strains, is not a plausible explanation. Additionally, as pointed out by Bitzek and Gumbsch [14] in their recent MD work, and previously stated by George and Michot [13], and confirmed by X-ray tomography results [61,62], the more commonly observed dislocation source in crack propagation is a consequence of emission of multiple Burgers vectors on different glide planes at once, in other words, multi-slip plane activity, which explains the misalignment between MSCDFMs and slip planes.

4.4. Relationship between cyclic and monotonic MSCDFM behavior

In order to investigate the difference of the MSCDFMs behavior between monotonic and cyclic loading conditions, a simulation performing cyclic loading of the *IN100* realization with a crack length $a = 0.91$ μm has been performed. Fig. 15 depicts the macroscopic stress/strain response of the aforementioned microstructure for a strain controlled cyclic load with a strain amplitude $R_\varepsilon = 0$, a maximum strain $\varepsilon_{33} = 3\%$ for a total of 51 cycles. It should be noted that to emphasize the stabilization of the hysteresis loop (the difference in macroscopic behavior between cycle 50 and 51 is not noticeable), only a few cycle are plotted. Also, according to Tóth et al. [43], when the hysteresis loop stabilizes, very small plastic deformations are induced to the material and the plasticity is concentrated into non-favorable microstructure features. Moreover, recognizing that the stabilization of the hysteresis loop also implies a stabilization of plastic strain relaxation, we observe a "saturation-like" behavior of the MSCDFMs. This is shown in Fig. 16, where the spatial average value of each MSCDFM at maximum strain, normalized with respect to the maximum MSCDFM value found in the crack plane at maximum strain ($\varepsilon_{33} = 3\%$) for cycle 51, is plotted against the numbers of cycles. Furthermore, the spatial average is calculated on voxels

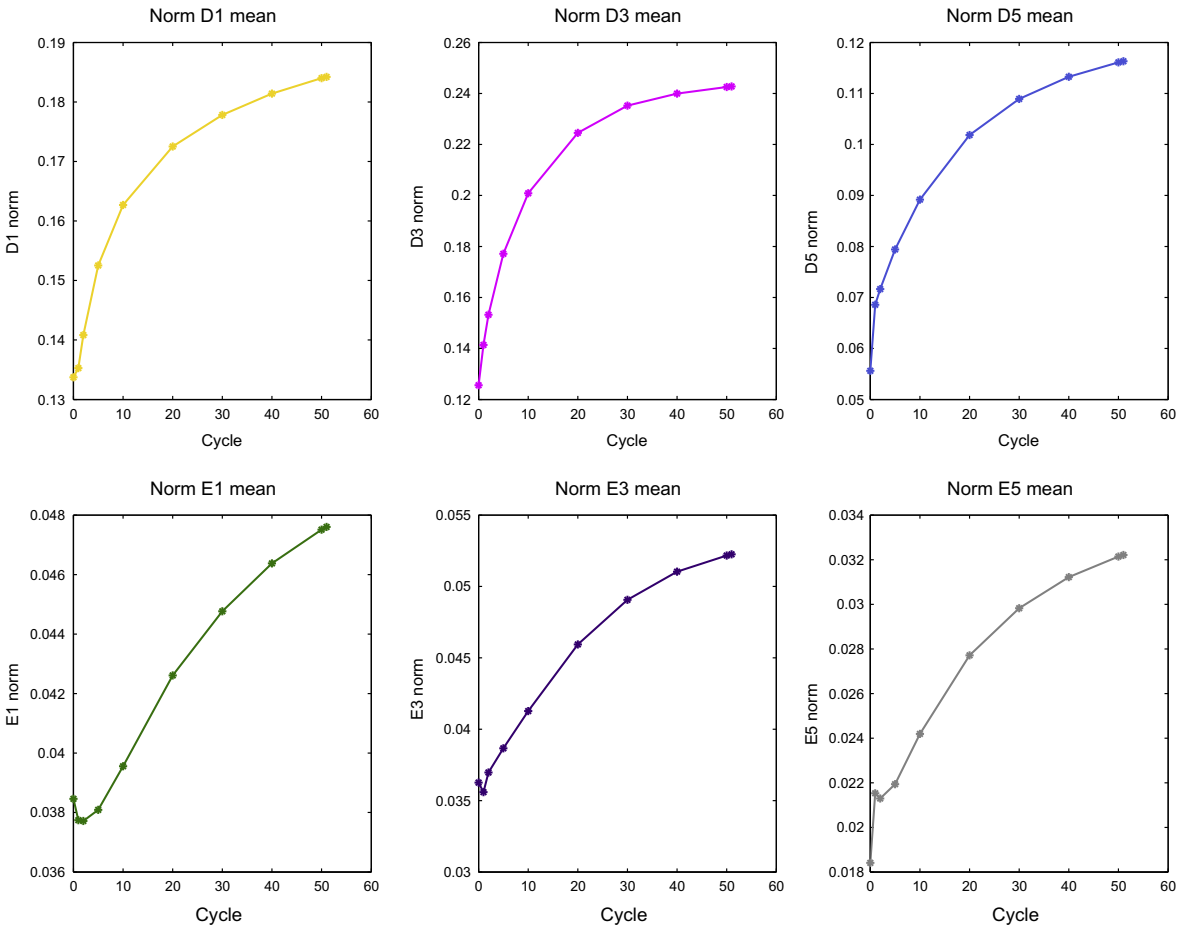

Fig. 16. Average normalized value of different MSCDFMs vs. cycle number. The normalization parameter for each MSCDFM is its maximum value found on the crack plane at cycle 51. It should be noted how all MSCDFMs show a saturation behavior through cycling.

embedded inside an idealized toroid in front of the crack tip, with the same dimension and location for all MSCDFMs. Comparing the different plot in Fig. 16, it is remarkable to see how, despite their different formulation, all the 6 MSCDFMs show the same "saturation-like" behavior, even if reached at different rates. This does not mean that all MSCDFMs will reach a stable value, in fact, looking back at Fig. 15, the small nonlinear portion of the macroscopic stress/strain curve at higher-cycles is due to the continued existence of kinematic hardening, i.e. the "hard-grains" are still in elastic regime, while "soft grains" continue to accumulate damage. This trend suggests an established MSCDFM pattern with cyclic evolution, but does not suggest that the MSCDFMs will completely saturate.

To indicate the stability of the MSCDFM parameters with respect to cycle number, a contour plot of the normalized E5 value with respect to its maximum value found on the *XY-plane* (see Fig. 3(b)) at maximum strain is depicted in Fig. 17 at different cycles: (a–d) shows the behavior of normalized E5 through the *XY-plane* (see Fig. 3(b)) respectively at cycle number 0, 5, 10, 50; while (e–h) depicts the associated behavior in the *YZ-plane* (see Fig. 3(b)). From these contour plots, we observe the consistency of the "hot spots" of the analyzed MSCDFMs through cycling. It should be noted that similar result have been obtained for all the other MSCDFMs, but as aforementioned in the previous section, different MSCDFMs lead to different "hot-spot" locations. The stability of the MSCDFMs is critical for damage analysis and motivates the present study for quasi-static crack growth from monotonic load results. Thus, from cyclic loading, we can obtain inferences of the MSCDFM behavior and associated relevance to crack growth, defined during the first loading cycle.

4.5. Relationship with short crack growth

During the last decade, the evaluation of MSCDFMs has emerged within computational materials modeling as a metric for characterizing the driving force for both crack propagation and nucleation. Castelluccio and McDowell [25] found a direct relationship between the Fatemi–Socie parameter and the crack tip displacement. Hochhalter et al. [26] investigated

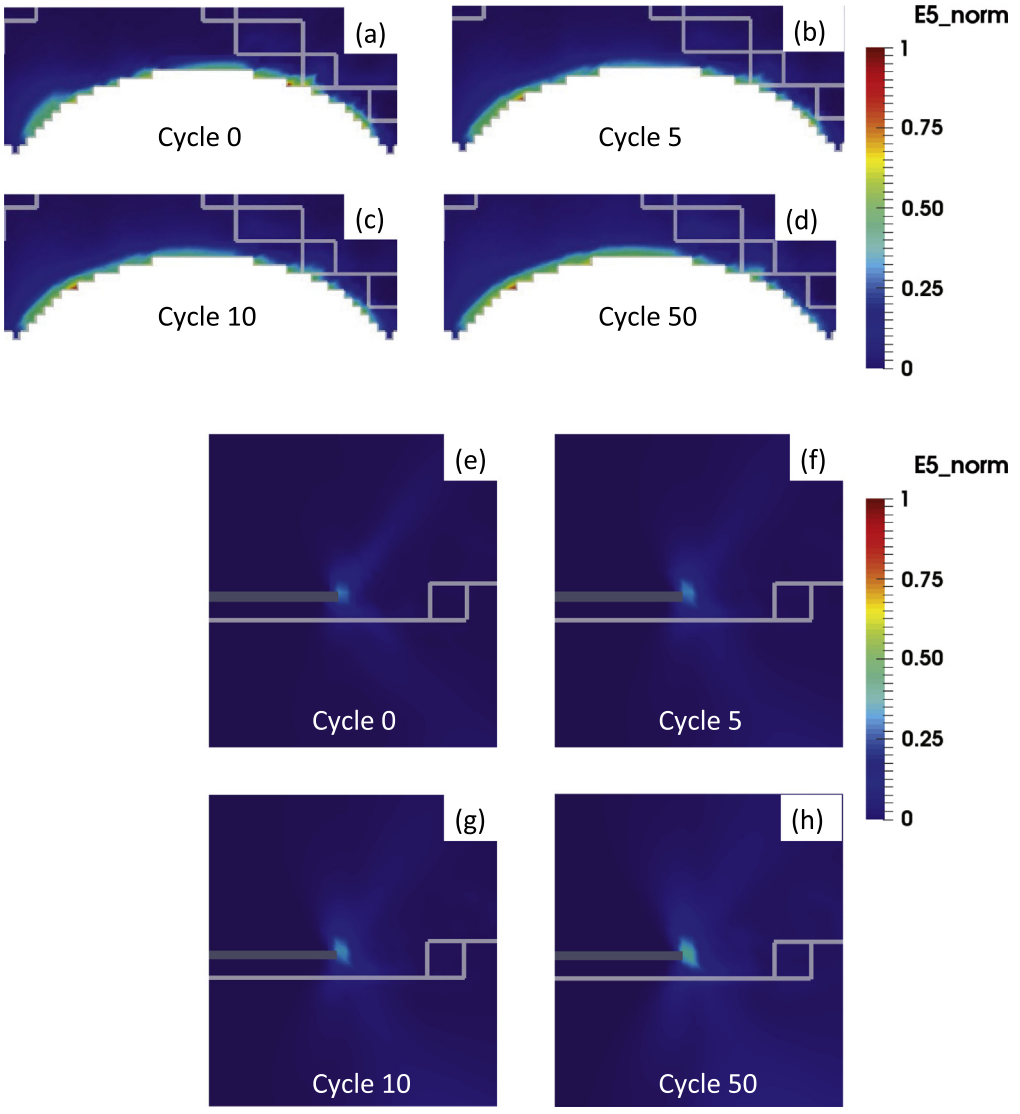

Fig. 17. Contour plot of normalized E5 value evolution on the *YZ-plane* (see Fig. 3(b)) as a function of cycle number (0, 5, 10, 50, respectively) at maximum strain, i.e. $\varepsilon = 3\%$: (a–d) the crack plane, (e–h) plane perpendicular to crack plane passing through the ellipse minor axes.

different MSCDFMs for crack initiation and also hypothesized the use of MSCDFMs for a linear prediction of damage accumulation. Also, Guilhem et al. [11] also investigated different MSCDFMs for crack nucleation.

In the well-known Paris plot of fatigue crack growth, i.e. the da/dN vs. ΔK chart, region 1 is typically associated with short crack growth. In this region, the size of the crack is smaller than the prominent features in the microstructure. Hence, the plastic zone size ahead of the crack tip has strong interactions with the strain fields produced by the defects in the microstructure. For this reason, region 1 of short crack growth is strongly influenced by the microstructure. However, there is no theory available to predict fatigue crack growth based upon the local microstructure, especially since stress intensity factors depend on the crack length, applied stress, and geometry of the crack, i.e. none of these parameters accounting for microstructure. Furthermore, since engineering alloys usually have a distribution of microstructural attributes, we expect variability in the short fatigue crack behavior, especially in threshold measurements [63]. For these reasons, it is important to quantify the variations in the MSCDFM near the crack tip with respect to variability in the microstructure.

In the work of McEvily and Boettner [2] it was found that the SCG rate in a single crystal is orientation-dependent. The grain orientations leading to higher degrees of work-hardening are associated with an increase in growth rates. Meanwhile, in polycrystalline materials, crack advancement is a selective process based on favorably oriented grains. Yoder et al. [5] investigated the relationship between average grain size and the value of ΔK_{th}, showing how the latter increases proportionally to the square root of the average grain size. Wilkinson [8] showed the dependence between SCG rate and the location of the crack tip with respect to nearby GBs, specifically displaying the influence of GB misorientation on SCG rate. These

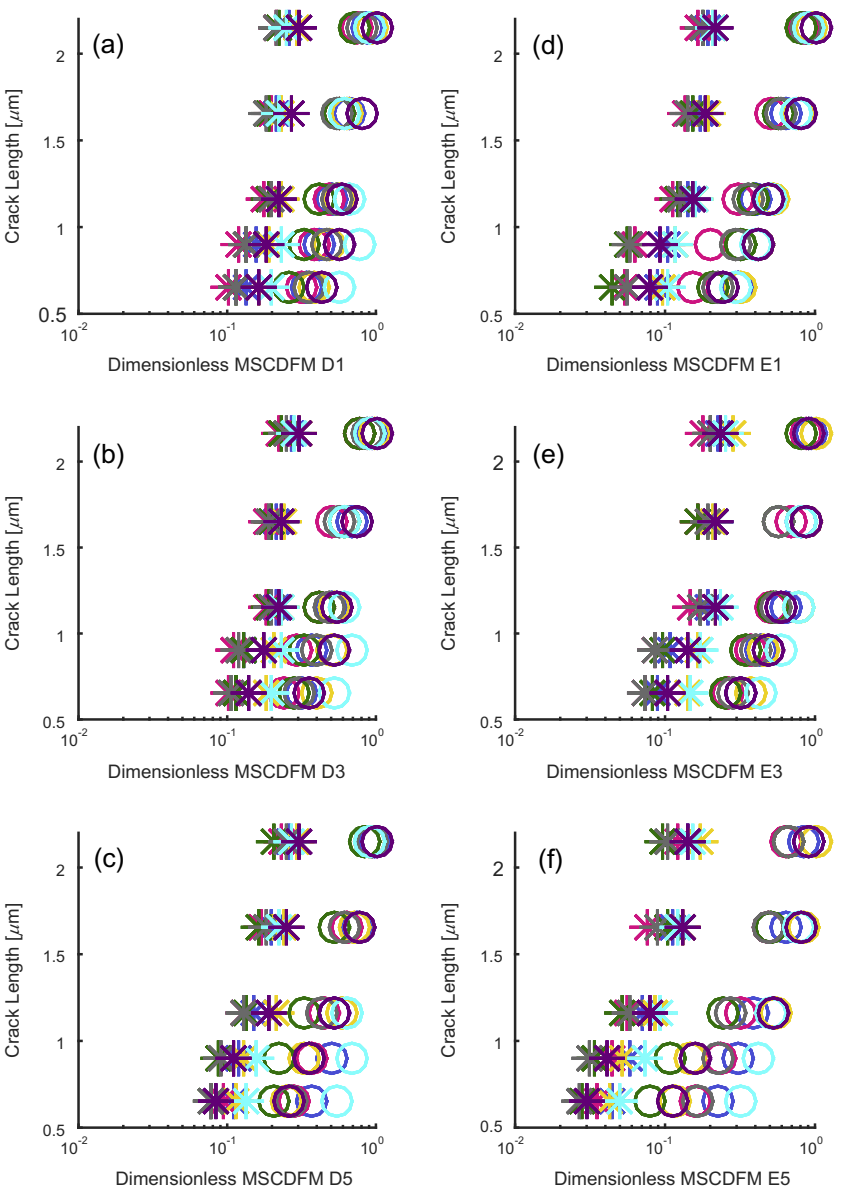

Fig. 18. Shape of nondimensionalized MSCDFMs (w.r.t. their maximum) plotted against crack length. The value in the charts are obtained utilizing the maximum value of each MSCDFM for each realization, at each strain level, for each crack length, and then normalizing with the overall maximum value. Stars represents a global strain of 0.32% (middle of linear elastic zone), while open circles represents a strain of 0.56% beginning of elasto-plastic zone.

microstructure variability parameters will influence slip character, strain accumulation, irreversibility and therefore growth rate, modifying the ΔK_{th} value due to the following phenomena: (i) the *cracked grain* orientation influences the resolved shear stress on slip systems, introducing variability in both strain accumulation and slip character. As a result, the shapes and surfaces of the plastic zone ahead of the crack tip vary within the *cracked grain*, and eventually in its neighbors, thereby modifying the threshold value for crack propagation; (ii) The grain size defines the density of GBs within a volume of material. Consequently, this interaction between the stress field near the crack tip and the GBs could work-harden the material by dislocation emission [64], thereby increasing the SCG rate; (iii) The distance between GBs and crack tip is another crucial parameter, thus introducing different mean-free path lengths for dislocations motion from a crack tip impinging upon a GB, thereby affecting slip transfer and, in turn, irreversibility.

From a crystal plasticity perspective, the influence of all the previously parameters can be taken into account, by accounting locally for slip accumulation and resolved shear stress. For these reasons, the use of MSCDFMs (Eqs. (6)–(11)) constitutes a good choice to account for variability in ΔK_{th} value. Moreover, the Fatemi–Socie parameter (which may be considered as the original MSCDFM), was conceived analogous to a stress intensity factor, ΔK [65]. For this reason, we plot the normalized

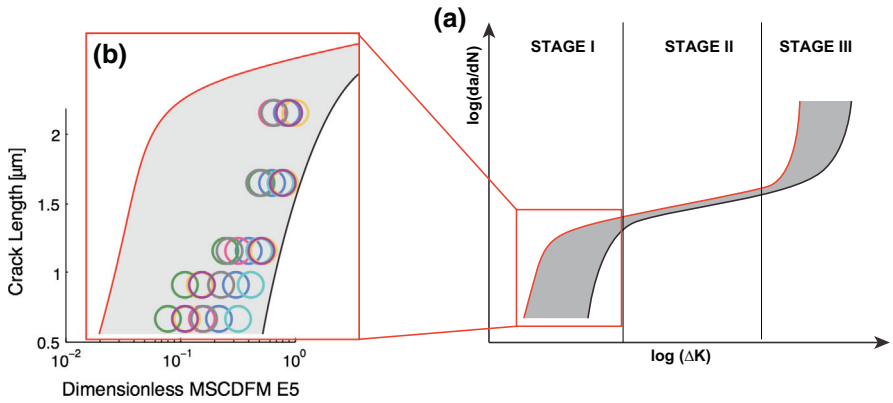

Fig. 19. Analogous behavior between the shape of E5 and small crack behavior. The small crack variability can be related to our quasi static SCG analysis through this indicator parameter that takes into account critical plane dissipated energy as major indicator of damage nucleation and consequent failure.

MSCDFMs vs. crack size, which is analogous of the Paris diagram (da/dN vs ΔK). Fig. 18 depicts the crack length vs. the log values of the normalized MSCDFMs (for the six MSCDFMs analyzed in this study) at different strain level ($\varepsilon_{33} = 0.32\%$ represented by stars, and $\varepsilon_{33} = 0.56\%$ represented by circles) for all realizations. For each MSCDFM, the normalization parameter is the maximum value reached in the analyzed configuration. It should be noted that by decreasing the crack length, the variability increases, and vice versa. This behavior is exemplified in MSCDFMs based on critical plane damage accumulation, namely D5 and E5, which allow identification of the transition between microstructural short cracks (dependent on the microstructure) and macroscopically short crack (less sensitive to microstructure variability). The shape of the analogous normalized MSCDFM compared to the crack length is similar to the variability in short crack behavior as originally constructed by Newman et al. [66], which depicts the variability in SCG rates for a given stress intensity factors. The similarity in shapes of these diagrams is most pronounced in the E5 MSCDFM, which emphasizes the choice of E5 MSCDFM as a suitable reference parameter. Fig. 19 shows a possible relation between SCG behavior and the chosen E5 MSCDFM. In Fig. 19(a), the complete fatigue crack propagation behavior is shown, as well characterized in literature [67]. The variability is more a noticeable in stages 1 and 3 as shown by the shaded zones. Fig. 19(b) displays an enlargement of stage 1, in which we superimpose the values of the E5 MSCDFMs calculated in these simulations, thus displaying the analogy between variability commonly observed in SCG and the reference parameter (E5 MSCDFM values as influenced by the various microstructure realizations).

4.6. Source of uncertainty

In each simulation and the associated data analysis, there are different sources of errors, which can manifest and propagate throughout the analysis. The modeling errors have been addressed in Sections 2 and 3. For the role of the crack geometry, it is noted that an equi-spaced grid is required by the EVP–FFT model, thus resulting in a blunt crack. In fact, while it is possible to reproduce a smooth profile of the crack tip in the crack plane, it is not possible to reproduce a geometrically sharp crack. However, the modeling results display the characteristic butterfly shape of the plastic zone (see Fig. 6). A specific study comparing the EVP–FFT and EVP–FEM should be done in order to quantify the difference of model refinement near the crack tip. We should also remind that, while we used an integral formulation to calculate the misalignment between MSCDFMs and both principal stress axis and slip planes, we did not discard the data present in the proximity of the tip. The local influence of computations near a singularity (i.e. the crack tip) are not necessarily precise due to numerical approximation, hence a possible over/under estimation of the field of interest is possible. For sake of completeness, the same analysis should be repeated utilizing nonlocal MSCDFMs in order to quantify the error.

5. Conclusions

Variability in the microstructure is inherent to engineering alloys, and it manifests itself in variability in the short crack (SC) behavior, as:

- During early stages of crack propagation, the stress fields produced by the crack are small compared with the stress fields associated with microstructural features such as grain boundaries, thus the microstructure plays a crucial role for prediction of fatigue life. This work addresses variability in the microstructure as a means to understand unfavorable microstructure features that facilitate SCG.
- Similar orientation can lead to very different behavior ahead of the crack tip in both macroscopic (e.g. von Mises stress) and microscopic (e.g. active slip systems) length scales. Crack propagation is a phenomenon governed by extreme values of the resolved shear stress and the resolved plastic shear strain reached in the proximity of the crack tip.

- The influence of the cracked grain orientation and of the crack length can be observed, not only directly ahead of the crack tip, but also in adjacent grains ahead of the crack tip. Thus, the clusters of grains ahead of the crack tip must be analyzed to determined SCG behavior.
- Thus, the clusters of grains ahead of the crack tip must be analyzed to determined SCG behavior.
- By successfully addressing microstructure variability, we elucidate the well-known phenomenon of scatter in the crack growth rates in stage 1 of the conventional Paris diagram.
- From this analysis, there is a critical need of a microstructure-sensitive definition of the driving force for SCG:
- Microstructure features affect the distribution of the stress fields at microscopic level, leading to different slip system activation that will in turn influence slip irreversibility and associated SCG behavior/rate.
- From the analysis of the six different fatigue indicator parameters (MSCDFM) analyzed, we identified E5 as the best candidate for a SCG driving force. The parameter E5 accounts for energy dissipation on the critical plane.
- At low strain levels, the direction connecting the maximum values of the MSCDFM ahead of the crack tip is driven by principal stress axes, since elastic strains dominate. At higher strain levels, the direction from the crack tip to the maximum MSCDFM values has a good alignment with the critical plane of maximum shear stress. In this case, the damage accumulation in the vicinity of the crack tip is a consequence of the accumulation of plastic strain on multiple slip systems, local grain rotation, and energy dissipation.
- Fatigue behavior and SCG path are strongly influenced by the interaction between stress/strain fields induced by the crack and those induced by the microstructure features. By analyzing the interaction between these stress fields, we can get insights on fracture mechanisms and crack paths, such as grain shielding and crack bifurcation.

Acknowledgements

The authors would like to thank Prof. Enrico Troiani for his help during the exchange program between University of Bologna and Purdue University. AR and MDS gratefully acknowledge funding from the Air Force Office of Scientific Research under Contract No. FA9550-14-1-0284. RAL acknowledges support from the Joint DoD/DOE Munitions Technology Programs. Also, the authors graciously acknowledge technical support and advice from the BlueQuartz Software team, Dr. Michael A. Groeber and Mr. Michael A. Jackson.

Appendix A. Supplementary data

Supplementary data associated with this article can be found, in the online version, at http://dx.doi.org/10.1016/j.engfracmech.2015.03.001.

References

[1] Paris PC, Gomez MP, Anderson WE. A rational analytic theory of fatigue. Trend Engmg 1961;13:9–14.
[2] McEvily Jr AJ, Boettner RC. On fatigue crack propagation in f.c.c. metals. Acta Metall 1963;11:725–43.
[3] Neumann P. New experiments concerning the slip processes at propagating fatigue cracks. Acta Metall 1974;22:1155–65.
[4] Rice JR, Thomson R. Ductile versus brittle behaviour of crystals. Philos Mag 1974;29:73–97.
[5] Yoder GR, Cooley LA, Crooker TW. Quantitative analysis of microstructural effects on fatigue crack growth in Widmanstatten Ti–6Al–4V and Ti–8Al–1Mo–1V. Engng Fract Mech 1979;11:805–16.
[6] Navarro A, de los Rios ER. A microstructurally-short fatigue crack growth equation. Fatigue Fract Engng Mater Struct 1988;11:383–96.
[7] Asaro RJ. Crystal plasticity. Trans ASME J Appl Mech 1983;50:921–34.
[8] Wilkinson AJ. Modelling the effects of texture on the statistics of stage I fatigue crack growth. Philos Mag A 2001;81:841–55.
[9] Ferrie E, Sauzay M. Influence of local crystallographic orientation on short crack propagation in high cycle fatigue of 316 LN steel. J Nucl Mater 2009;386–388:666–9.
[10] Potirniche GP, Daniewicz SR, Newman JC. Simulating small crack growth behaviour using crystal plasticity theory and finite element analysis. Fatigue Fract Engng Mater Struct 2004;27:59–71.
[11] Guilhem Y, Basseville S, Curtit F, Stéphan JM, Cailletaud G. Investigation of the effect of grain clusters on fatigue crack initiation in polycrystals. Int J Fatigue 2010;32:1748–63.
[12] Sangid MD, Maier HJ, Sehitoglu H. An energy-based microstructure model to account for fatigue scatter in polycrystals. J Mech Phys Solids 2011;59:595–609.
[13] George A, Michot G. Dislocation loops at crack tips: nucleation and growth-an experimental study in silicon. Eur. Res. Conf. Plast. Mater. – Fundam. Asp. Dislocation interact. Low-energy dislocation struct. III, 30 August to 4 September 1992, vol. A164. 1st–2nd ed., Switzerland; 1993. p. 118–34.
[14] Bitzek E, Gumbsch P. Mechanisms of dislocation multiplication at crack tips. Acta Mater 2013;61:1394–403.
[15] Zhang J, Ghosh S. Molecular dynamics based study and characterization of deformation mechanisms near a crack in a crystalline material. J Mech Phys Solids 2013;61:1670–90.
[16] Sangid MD, Ezaz T, Sehitoglu H, Robertson IM. Energy of slip transmission and nucleation at grain boundaries. Acta Mater 2011;59:283–96.
[17] Irwin GR. Analysis of stresses and strains near end of crack traversing plate. Am Soc Mech Engng – Trans – J Appl Mech 1957;24:361–4.
[18] Abraham FF, Walkup R, Gao H, Duchaineau M, Diaz De La Rubia T, Seager M. Simulating materials failure by using up to one billion atoms and the world's fastest computer: work-hardening. Proc Natl Acad Sci 2002;99:5783–7.
[19] Argon AS. Mechanics and physics of brittle to ductile transitions in fracture. Trans ASME J Engng Mater Technol 2001;123:1–11.
[20] Giannattasio A, Roberts SG. Strain-rate dependence of the brittle-to-ductile transition temperature in tungsten. Philos Mag 2007;87:2589–98.
[21] Gumbsch P, Riedle J, Hartmaier A, Fischmeister HF. Controlling factors for the brittle-to-ductile transition in tungsten single crystals. Science (80–) 1998;282:1293–5.
[22] Mughrabi H. Cyclic slip irreversibilities and the evolution of fatigue damage. Metall Mater Trans B Process Metall Mater Process Sci 2009;40:431–53.
[23] Bennett VP, McDowell DL. Polycrystal orientation distribution effects on microslip in high cycle fatigue. Int J Fatigue 2003;25:27–39.

[24] Fatemi A, Socie DF. Critical plane approach to multiaxial fatigue damage including out-of-phase loading. Fatigue Fract Engng Mater Struct 1988;11:149–65.
[25] Castelluccio GM, McDowell DL. Assessment of small fatigue crack growth driving forces in single crystals with and without slip bands. Int J Fract 2012;176:49–64.
[26] Hochhalter JD, Littlewood DJ, Christ Jr RJ, Veilleux MG, Bozek JE, Ingraffea AR, et al. A geometric approach to modeling microstructurally small fatigue crack formation: II. Physically based modeling of microstructure-dependent slip localization and actuation of the crack nucleation mechanism in AA 7075-T651. Model Simul Mater Sci Engng 2010;18:045004. 33pp.
[27] Lebensohn RA, Kanjarla AK, Eisenlohr P. An elasto-viscoplastic formulation based on fast Fourier transforms for the prediction of micromechanical fields in polycrystalline materials. Int J Plast 2012;32–33:59–69.
[28] Moulinec H, Suquet P. A fast numerical method for computing the linear and nonlinear mechanical properties of composites. Comptes Rendus l'Academie Des Sci Ser II 1994;318:1417–23.
[29] Moulinec H, Suquet P. A numerical method for computing the overall response of nonlinear composites with complex microstructure. Comput Methods Appl Mech Engng 1998;157:69–94.
[30] Michel JC, Moulinec H, Suquet P. A computational method based on augmented Lagrangians and fast Fourier transforms for composites with high contrast. Comput Model Engng Sci 2000;1:79–88.
[31] Michel JC, Moulinec H, Suquet P. A computational scheme for linear and non-linear composites with arbitrary phase contrast. 5th US Natl Congr Comput Mech 4–6 August 1999, vol. 52. UK: Wiley; 2001.
[32] Brenner R, Lebensohn RA, Castelnau O. Elastic anisotropy and yield surface estimates of polycrystals. Int J Solids Struct 2009;46:3018–26.
[33] Lebensohn RA. N-site modeling of a 3D viscoplastic polycrystal using fast Fourier transform. Acta Mater 2001;49:2723–37.
[34] Lebensohn RA, Brenner R, Castelnau O, Rollett AD. Orientation image-based micromechanical modelling of subgrain texture evolution in polycrystalline copper. Acta Mater 2008;56:3914–26.
[35] Lebensohn RA, Montagnat M, Mansuy P, Duval P, Meysonnier J, Philip A. Modeling viscoplastic behavior and heterogeneous intracrystalline deformation of columnar ice polycrystals. Acta Mater 2009;57:1405–15.
[36] Lee SB, Lebensohn RA, Rollett AD. Modeling the viscoplastic micromechanical response of two-phase materials using Fast Fourier Transforms. Int J Plast 2011;27:707–27.
[37] Adams BL, Wright SIL, Kunze K. Orientation imaging: the emergence of a new microscopy. Metall Trans A 1993;24:819–31.
[38] Lienert U, Li SF, Hefferan CM, Lind J, Suter RM, Bernier JV, et al. High-energy diffraction microscopy at the advanced photon source. JOM 2011;63:70–7.
[39] Eisenlohr P, Diehl M, Lebensohn RA, Roters F. A spectral method solution to crystal elasto-viscoplasticity at finite strains. Int J Plast 2013;46:37–53.
[40] Tomé CN, Canova GR, Kocks UF, Christodoulou N, Jonas JJ. The relation between macroscopic and microscopic strain hardening in FCC polycrystals. Acta Metall 1984;32:1637–53.
[41] Voce E. The relationship between stress and strain for homogeneous deformation. J Inst Met 1948;74:536–62.
[42] Rice JR. Inelastic constitutive relations for solids: an internal-variable theory and its application to metal plasticity. J Mech Phys Solids 1971;19:433–55.
[43] Tóth LS, Molinari A, Zouhal N. Cyclic plasticity phenomena as predicted by polycrystal plasticity. Mech Mater 2000;32:99–113.
[44] Hochhalter JD, Littlewood DJ, Veilleux MG, Bozek JE, Maniatty AM, Rollett AD, et al. A geometric approach to modeling microstructurally small fatigue crack formation: III. Development of a semi-empirical model for nucleation. Model Simul Mater Sci Engng 2011;19:035008.
[45] Choi YS, Groeber MA, Turner TJ, Dimiduk DM, Woodward C, Uchic MD, et al. A crystal-plasticity FEM study on effects of simplified grain representation and mesh types on mesoscopic plasticity heterogeneities. Mater Sci Engng A 2012;553:37–44.
[46] Pyle DM, Lu J, Littlewood DJ, Maniatty AM. Effect of 3D grain structure representation in polycrystal simulations. Comput Mech 2012;52:135–50.
[47] Kanit T, Forest S, Galliet I, Mounoury V, Jeulin D. Determination of the size of the representative volume element for random composites: statistical and numerical approach. Int J Solids Struct 2003;40:3647–79.
[48] AFRL–WPAFB. SMALL IN100; 2004.
[49] BlueQuartz. Dream3d 2012; 2012.
[50] Groeber M. Development of an automated characterization- representation framework for the modeling of polycrystalline materials in 3D, 2007.
[51] Fromm BS, Chang K, McDowell DL, Chen L-Q, Garmestani H. Linking phase-field and finite-element modeling for process–structure–property relations of a Ni-base superalloy. Acta Mater 2012;60:5984–99.
[52] Milligan WW, Orth EE, Schirra JJ, Savage MF. Effects of microstructure on the high temperature. Superalloys 2004. In: Proc. Tenth Int. Symp. Superalloys Spons. by TMS Seven Springs Int. Symp. Committee, Coop. with TMS High Temp. Alloy. Comm. ASM Int., 2004. p. 331–9.
[53] Shenoy M, Tjiptowidjojo Y, McDowell DL. Microstructure-sensitive modeling of polycrystalline IN 100. Int J Plast 2008;24:1694–730.
[54] Rollett AD, Lebensohn RA, Groeber M, Choi Y, Li JS, Rohrer GS. Stress hot spots in viscoplastic deformation of polycrystals. Model Simul Mater Sci Engng 2010;18.
[55] Lee TC, Robertson IM, Birnbaum HK. Prediction of slip transfer mechanisms across grain boundaries. Scr Metall 1989;23:799–803.
[56] Moulinec H, Suquet P. Intraphase strain heterogeneity in nonlinear composites: a computational approach. Eur J Mech A/Solids 2003;22:751–70.
[57] Sadananda K, Glinka G. Dislocation processes that affect kinetics of fatigue crack growth. Symp Defects Deform Cryst Solids. 2–6 March 2003, vol. 85. UK: Taylor & Francis; 2005.
[58] Brown MW, Miller KJ. A theory for fatigue failure under multiaxial stress–strain conditions. Proc Inst Mech Engng 1973;187:745–55.
[59] Tschopp MA, McDowell DL. Influence of single crystal orientation on homogeneous dislocation nucleation under uniaxial loading. J Mech Phys Solids 2008;56:1806–30.
[60] Korsunsky AM, Dini D, Dunne FPE, Walsh MJ. Comparative assessment of dissipated energy and other fatigue criteria. Int J Fatigue 2007;29:1990–5.
[61] Michot G. Interaction of a dislocation with a crack tip: from stimulated emission to avalanche generation. Acta Mater 2011;59:3864–71.
[62] Scandian C, Azzouzi H, Maloufi N, Michot G, George A. Dislocation nucleation and multiplication at crack tips in silicon. Phys Status Solidi Appl Res 1999;171:67–82.
[63] Taylor D, Knott JF. Fatigue crack propagation behaviour of short cracks; the effect of microstructure. Fatigue Fract Engng Mater Struct 1981;4:147–55.
[64] Sangid MD, Pataky GJ, Sehitoglu H, Rateick RG, Niendorf T, Maier HJ. Superior fatigue crack growth resistance, irreversibility, and fatigue crack growth–microstructure relationship of nanocrystalline alloys. Acta Mater 2011;59:7340–55.
[65] Socie DF. Personal communication; 2013.
[66] Newman JC, Phillips EP, Swain MH. Fatigue-life prediction methodology using small-crack theory. Int J Fatigue 1999;21:109–19.
[67] Hertzberg RW. Deformation and fracture mechanics of engineering materials, vol. 89. New York: Wiley; 1996.